

The diffuselet concept for scalar mixing

Patrice Meunier^{1,†} and Emmanuel Villermaux¹

¹Aix Marseille Univ, CNRS, Centrale Marseille, IRPHE, Marseille, France

(Received 12 April 2022; revised 5 August 2022; accepted 29 August 2022)

The advection–diffusion of a small surface element of scalar in three dimensions (or of a small line element in two dimensions) is solved analytically thanks to the Ranz transform (Ranz, *AIChE J.*, vol. 25, issue 1, 1979, pp. 41–47). As the quantum or elementary brick of any complex mixture, we call this element a diffuselet. Its evolution is computed numerically from the integration of the velocity gradient along the trajectory, as classically done for the Lyapunov exponents. The concentration profile across the diffuselet is obtained from the product of its initial orientation with a dimensionless tensor. Averaging over all initial orientations yields simple formulae for the mean scalar variance and the scalar probability distribution function (p.d.f.). This technique is then applied to two-dimensional and three-dimensional sine flows, in excellent agreement with direct numerical simulations. For these simple flows, the temporal integration is obtained analytically leading to simple integrals for the scalar variance and p.d.f. Statistics of stretching rates are calculated as well. The Lyapunov exponent is close to the value for short-time correlated flows (Kraichnan, *J. Fluid Mech.*, vol. 64, issue 4, 1974, pp. 737–762) in the case of a small displacement during each step; it is close to the value for a simple shear in the case of a large displacement. The p.d.f. of stretching factors are log normal with a ratio between the mean and the variance equal to half the dimension of space for small displacements (in agreement with Kraichnan, *J. Fluid Mech.*, vol. 64, issue 4, 1974, pp. 737–762), but increases strongly for large displacements.

Key words: coupled diffusion and flow, computational methods

1. Introduction

Scalar mixing remains extremely difficult to solve numerically for weak diffusivities. We provide here a new numerical method in three dimensions to calculate the evolution of small blobs of diffusing scalar advected by a flow.

The advection–diffusion of a scalar in a flow is ubiquitous, including for problems at the Earth scale. In the atmosphere these scalars can be temperature, humidity or CO₂

† Email address for correspondence: patrice.meunier@univ-amu.fr

concentration, with an identified major impact on climate both on a short and long term basis (Manabe & Wetherald 1975). In oceans temperature, salinity, CO₂ concentration, nutrients and micro-algae are examples of scalars whose patterns are sensitive to the general, and local circulation (Munk 1966; Wunsch & Ferrari 2004), with intriguing micro-structures (Hayes, Joyce & Milliard 1975).

More generally, mixing is at the crossroads of many different well-classified areas of science. The reason is that one often needs to mix to make something, i.e. a new product, a chemical reaction, an homogeneous blend, a fast combustion, etc or one needs to understand how nature mixes or has mixed to gain information on, for example, the size of a pollutant spot in a valley, the rate of destruction of ozone in the atmosphere or the earth mantle dynamics, or even to understand how an animal navigates in a complex field of nutriment (Celani, Villermaux & Vergassola 2014). Mixing is a key step in many complex man made or natural operations but often remains difficult to predict, even if the flow is known accurately. For example, simple laminar flows can create complex scalar structures such as strange attractors, recurrent patterns or fractals (Sukhatme & Pierrehumbert 2002; Rothstein, Henry & Gollub 1999).

Scalars in turbulence have been studied for a century, with an emphasis on spatial correlations, spectra and, following Kolmogorov's suggestion, the statistics of concentration differences or increments (see the perspectives in Shraiman & Siggia 2000; Warhaft 2000; Falkovich, Gawedzki & Vergassola 2001). The scalar energy spectrum has been predicted earlier by Obukhov (1941) and Corrsin (1951) to be prescribed by the hierarchy of time scales pre-existing in the stirring substrate, namely scaling like $k^{-5/3}$ in the inertial range, a prediction confirmed experimentally (see, e.g. Gibson & Schwarz 1963), and scaling like k^{-1} for scalars with small molecular diffusivity in the dissipative range of scales (Batchelor 1959).

One point scalar probability distribution functions (p.d.f.s) – as opposed to the p.d.f. of scalar increments – are in general believed to be, and sometimes actually observed to be close to Gaussian (Sreenivasan *et al.* 1980; Tavoularis & Corrsin 1981; Jayesh & Warhaft 1991), like for the velocity field. However, measurements with narrow p.d.f.s centred around the mean are representative of the well-mixed limit, in the late stages of the mixtures evolution. By contrast, plumes released in a strongly turbulent environment (a jet) soon resolving into a set of disjointed stretched sheets are known to exhibit skewed, absolutely non-Gaussian p.d.f. shapes (Duplat, Innocenti & Villermaux 2010a) with an exponential tail reflecting the distribution of mixing times (Villermaux 2019). For other types of injection, for example, within a mean scalar gradient, Gollub *et al.* (1991) and Jayesh & Warhaft (1991) have observed exponential tails, also interpreted by a distribution of mixing times (Pumir, Shraiman & Siggia 1991). These exponential tails are even more pronounced in the p.d.f. of the scalar gradient (Warhaft 2000), or of scalar increments in complex mixtures, a fact which has contributed to understanding their architecture (Le Borgne *et al.* 2017). Chaotic micro-mixers display a continuous transition of the p.d.f. between the characteristic initial \cup shape between the injection concentration and the zero concentration of the diluting stream, and a final rounded, close to Gaussian shape around the mean at late stages, nevertheless fitted with exponential tails (Simonet & Groisman 2005; Villermaux, Stroock & Stone 2008).

These non-Gaussian statistics are, in turbulence, called intermittency. There is, in fact, no reason why the Gaussian should be an ideal limit. On the contrary, the diversity of shapes reveals that the scalar p.d.f. depends on the nature of the injection (at small or large scale compared with the stirring scale), the nature of the flow (homogeneous or sheared

turbulence, with smooth or rough velocity increments), the space-fillingness of the scalar support (isolated sheets or confined mixture) and on the age of the mixture. But diversity does not imply that there is not a profound unity in the way mixtures are built (Villermaux 2019); they are made from quanta, or diffuselets, possibly interacting with each other depending on the nature of the flow (dispersing or confined). The overlap of many quanta leads to a scalar p.d.f. centred around the mean with few remnant fluctuations, while solitary or weakly interacting diffuselets present a broad, skewed decaying distribution of concentration with a fat tail, as in the present work.

It has been understood very early on that scalar diffusion is altered by the stretching of material lines and surfaces (Batchelor 1952). In an incompressible fluid, stretching of the scalar blob implies compression in its transverse direction, thus sharpening the concentration gradient and enhancing diffusion; this is the spirit of the Ranz (1979) transform. The stretching ability of the flow can be quantified by the pair dispersion, which measures the separation distance ℓ between two tracers advected by the flow. In a pioneering paper, Richardson (1922) measured that the square of this distance increases as t^3 . In homogeneous turbulence this law is now written as

$$\langle \ell^2 \rangle = g\epsilon t^3, \quad (1.1)$$

with ϵ the dissipation rate of kinetic energy and where the Richardson constant is equal to $g = 0.55$ (Richardson 1922; Salazar & Collins 2009; Buaria, Sawford & Yeung 2015). This behaviour is valid when the flow is rough, i.e. when the distance is larger than the Kolmogorov length scale (see, e.g. Falkovich *et al.* (2001) for this terminology). Below the Kolmogorov length scale (the smooth region of the flow), the distance between particles increases exponentially as classically obtained in chaotic flows (Aref 1984; Ottino 1989) and can be written as (Salazar & Collins 2009)

$$\langle \ell^2 \rangle \sim e^{2Bt/\tau_K}, \quad (1.2)$$

where $\tau_K = \nu/\epsilon$ is the Kolmogorov time. The Batchelor constant B was initially predicted to be equal to 0.4. In fact, it is smaller because of the finite correlation time of the flow. Using the assumption of a small correlation time suggested by Lundgren (1981), the Batchelor constant is $B = \sqrt{5}/15 \approx 0.15$ in good agreement with the value $B = 0.13$ found by DNS (Girimaji & Pope 1990). The p.d.f. of stretching rates is log normal as predicted by Kraichnan (1974) for a flow delta correlated in time and as measured in direct numerical simulations (DNS) (Girimaji & Pope 1990) in a real turbulent flow. Most of these studies focused on the stretching of line elements, but Girimaji & Pope (1990) also focused on the stretching of material surfaces. They found that the p.d.f. of the surface stretching rate is log normal with a mean Lyapunov exponent equal to $0.17/\tau_K$.

However, these studies do not address primarily the connection between scalar diffusion and the stretching properties of the flow. Experimentally, this is due to the difficulty to measure simultaneously the Lagrangian pair dispersion and the scalar concentration. Numerically, this is due to the very different nature of Lagrangian and Eulerian numerical methods. On one hand, Lagrangian methods consisting in following particles along their trajectory in the flow (Yeung 2002) do not consider the diffusion of the scalar. Brownian motion (Öttinger 1996) can be added to represent diffusion but it requires an enormous number of tracers that can be extremely costly (Götzfried *et al.* 2019). On the other hand, Eulerian methods cannot deal with weakly diffusing species in multiscale flows at high Reynolds and Schmidt numbers (Yeung, Donzis & Sreenivasan 2005; Schwertfimer & Manhart 2007) because of the refined resolution (spatial grid in particular) capabilities

it requires. However, the gap between these two techniques has been filled recently with the diffusive strip method (DSM) which advects small line elements in two dimensions (Meunier & Villermaux 2010). Diffusion is built-in analytically in this method based on the Ranz (1979) transform. This method has been extended to small surface elements by Martínez-Ruiz *et al.* (2018). We will show in this paper that these methods are very similar to the theoretical model of Balkovsky & Fouxon (1999), but simpler to implement numerically.

The present work is both a generalization of this method and an improvement of it to encode in an even more direct way the kinematics of the flow. Central to the concept of the diffuselet introduced here is the fact that what matters dynamically for the evolution of the scalar is the compression rate normal to material surfaces in the flow. Once it is known, all the properties of the scalar field (concentration profile, maximal concentration, gradient steepness) are known. Following a set of diffuselets in a flow or in a subset of the flow thus allows us to study their mixing capabilities and dynamics (distribution of elongation, of concentrations etc). In that sense, the diffuselet concept has some proximity with the flamelet representation of reactive mixtures in the combustion context (Peters 1984).

We describe first the roots of the diffuselet concept in the flow kinematics and explain their analogy with the dynamics of scalar gradients in deformable media (Corrsin 1953), then derive the essential formulae to compute from this method the distribution of elongations and concentrations, in any flow. In particular, we show how this method is, from its principle, equally capable to process two-dimensional (2-D) and three-dimensional (3-D) flows. We provide in this respect an explicit treatment of the 2-D and 3-D sine flows.

2. Definition of a diffuselet

2.1. From DNS to independent diffuselets

In order to characterize the mixing properties of a flow, it is convenient to introduce a blob of scalar and to follow its advection, diffusion and mixing, a procedure easily carried out experimentally leading to global measures such as scalar variance, p.d.f.s of scalar, spectra, correlation functions and so on, and also to quantify the transient evolution of these quantities as a function of the flow structure, or location of deposition of the blob in heterogeneous flows. Numerically, this procedure is also possible by solving the diffusion–advection equation

$$\frac{\partial c}{\partial t} + \mathbf{u} \cdot \nabla c = D \nabla^2 c \quad (2.1)$$

using DNS. An example is given in figure 1(a,b) where a strip of scalar is advected in a sine flow with random phases for a very small diffusivity $D = 10^{-6}$ (see Appendix A for further information on the numerical scheme). In some places, the strip is highly stretched such that its thickness decreases until it reaches the Batchelor scale $\sqrt{D/\gamma}$ at which diffusion starts to operate (γ being the stretching rate). For small diffusivities, the thicknesses are extremely small and require a very fine mesh. In this example, 8192 Fourier modes have been used in each direction, which requires a memory of 500 Mo. The CFD condition then imposes that the time step must also be very small. Such 2-D DNS are extremely expensive in terms of CPU time for small diffusivities. In three dimensions this

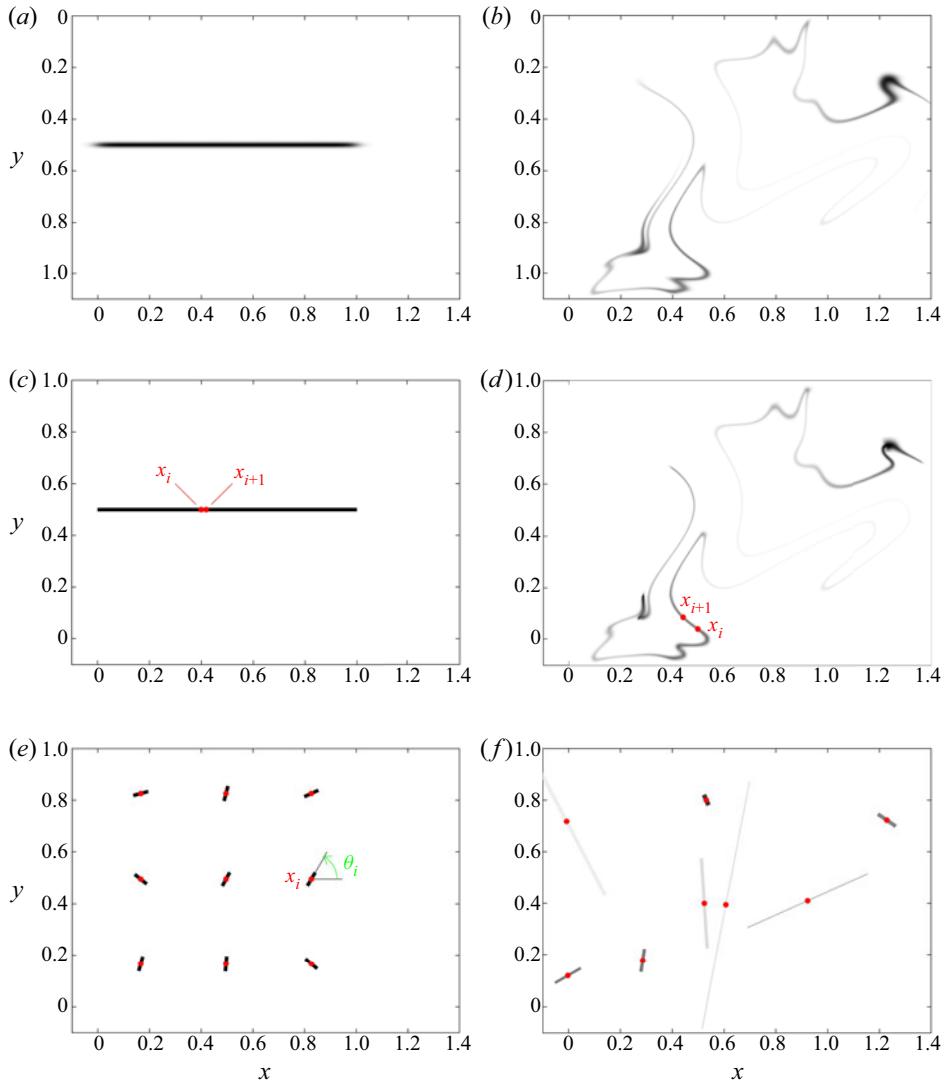


Figure 1. Different numerical methods used to quantify the mixing properties of a 2-D sine flow of period 1 with $U = 0.3$ and $D = 10^{-6}$ from $t = 0$ (a,c,e) to $t = 15$ (b,d,f). (a,b) Direct numerical simulation with 8192 Fourier modes in each direction. In (c,d) the initial concentration field is modelled as a strip defined by 1000 tracers advected using the DSM (Meunier & Villermaux 2010). In (e,f) nine independent diffuselets with initial orientation θ_i are advected as described in § 2.2.

method is extremely demanding even for moderate diffusivities and nearly impossible for small diffusivities.

In order to treat numerically the case of small diffusivities, the DSM has been proposed by Meunier & Villermaux (2010). The blob of scalar is modelled as a strip containing Lagrangian tracers which are advected by the flow

$$\frac{dx_i}{dt} = \mathbf{u}(x_i). \quad (2.2)$$

Each element of the strip $[x_i \ x_{i+1}]$ has a length $\delta\ell_i = |x_{i+1} - x_i|$ and a striation thickness s_i given by the incompressibility

$$s_i = \frac{s_0 \delta\ell_0}{\delta\ell_i}, \quad (2.3)$$

where s_0 and $\delta\ell_0$ are the initial thickness and length of each strip element. In this paper we will assume that the strip has initially a Gaussian profile (for simplicity) with a maximal concentration equal to 1 (from dimensionalisation). The characteristics of the strip can then be calculated easily using the Ranz transform (Ranz 1979) for each tracer. Indeed, defining a dimensionless time $\tau_i(t)$ given by

$$\frac{d\tau_i}{dt} = \frac{4D}{s_i^2}, \quad \text{with } \tau_i(t=0) = 1, \quad (2.4)$$

the maximal concentration at x_i is equal to $C_i = \tau_i^{-1/2}$ and the diffusive thickness (i.e. the Bachelor length) is equal to $s_i\sqrt{\tau_i}$. Indeed, the transverse profile of scalar is governed by a simple diffusion equation

$$\frac{\partial c_i}{\partial \tau_i} = \frac{1}{4} \frac{\partial^2 c_i}{\partial \xi_i^2} \quad (2.5)$$

for the new variables ($\xi_i = n_i/s_i$, τ_i), where n_i is the coordinate normal to the strip element $[x_i x_{i+1}]$. The transverse profile is thus given by

$$c_i(n_i) = \frac{1}{\sqrt{\tau_i}} \exp(-n_i^2/(s_i^2 \tau_i)). \quad (2.6)$$

An example is plotted in figure 1(d) after 15 periods of the sine flow. The maximal concentration and the thickness of the strip indeed corresponds to those found numerically by DNS. The computation is done with only 1000 tracers such that the computation time is only three minutes whereas it lasts a few hours for the DNS on the same computer. In this figure the strip has been plotted as a simple line with a modulated thickness and colour. It is possible to reconstruct the total scalar field on a mesh, as done in Meunier & Villermaux (2010). However, as mentioned earlier, the required mesh may become extremely fine when the diffusivity becomes small. Alternative methods have thus been developed in order to get the statistics (p.d.f., variance) and the spectra of the scalar field (see Meunier & Villermaux 2010).

Martínez-Ruiz *et al.* (2018) have generalized this 2-D method to three dimensions by considering diffusive surface elements rather than diffusive strip elements. The striation thickness is simply given by the incompressibility as

$$s_i = s_0 \frac{\delta A_0}{\delta A_i}, \quad (2.7)$$

where δA_i is the area of the surface element (being initially equal to δA_0). Defining the dimensionalised time $\tau_i(t)$ in the same way using (2.4) leads to the maximal concentration $C_i = \tau_i^{-1/2}$ and the diffusive thickness $s_i\sqrt{\tau_i}$.

However, dealing numerically with a sheet is much more complex than dealing with a strip since each surface element is connected to its neighbours in physical space, although this connection is not trivial in the structure of the numerical variables. Furthermore, refining the surface by adding surface elements, e.g. when the element's size or curvature is too large, adds another complexity. These complex techniques are necessary

to reconstruct the shape of the sheet. Fortunately, they are not necessary to obtain the p.d.f. and the variance of scalar in the diluted limit, i.e. when there is no self-aggregation of the folded strip or sheet. Indeed, each element can be solved independently since the diffusion (2.1) is linear for the concentration. The variance and the p.d.f. are then found as an ensemble average over all elements. Each element is the response to an initial insertion of scalar with a given striation thickness and an infinitely small area. This surface element may be called the diffuselet. It corresponds to the Green function of a surface rather than a point.

For independent diffuselets, the main problem is to calculate the striation thickness of each element without knowing the position of the neighbours. Indeed, the stretching between neighbouring points was used previously to calculate the length (in two dimensions) or the area (in three dimensions) of the diffuselet. This is what we propose in the next section.

2.2. General equations for a diffuselet

We first illustrate the concepts and the kinematic construction of the relevant quantities involved in the general discussion in two dimensions. We then extend this construction to the 3-D case. We finally apply the Ranz transform to incorporate diffusion with kinematics.

2.2.1. Concepts and kinematic construction in two dimensions

Let $\delta\ell = (\delta\ell_x, \delta\ell_y)$ be a vector of the plane $\{x, y\}$ between two material particles x_i and $x_i + \delta\ell$ advected by a velocity field $\mathbf{u}(x, t) = (u, v)$, as sketched in figure 2. The kinematic transport of $\delta\ell$ in (2.2) is such that $\dot{\delta\ell} = \mathbf{u}(x + \delta\ell) - \mathbf{u}(x)$ so that

$$\dot{\delta\ell}_x = \delta\ell_x \partial_x u + \delta\ell_y \partial_y u, \quad (2.8)$$

$$\dot{\delta\ell}_y = \delta\ell_x \partial_x v + \delta\ell_y \partial_y v \quad (2.9)$$

or, in compact form (Batchelor 1952; Cocke 1969), $\dot{\ell} = (\ell \cdot \nabla) \mathbf{u}$, also equivalently written in terms of the velocity gradient tensor $\delta\ell = (\overline{\nabla \mathbf{u}}) \delta\ell$, where

$$\overline{\nabla \mathbf{u}} = \begin{bmatrix} \partial_x u & \partial_y u \\ \partial_x v & \partial_y v \end{bmatrix}, \text{ with transpose } \overline{\nabla \mathbf{u}}^* = \begin{bmatrix} \partial_x u & \partial_x v \\ \partial_y u & \partial_y v \end{bmatrix}. \quad (2.10)$$

The stretching factor of the segment $\delta\ell$ or the pair dispersion rate of its extremities measured by $\delta\ell^2 = \delta\ell_x^2 + \delta\ell_y^2 = \delta\ell^* \delta\ell$ involves the operator $\overline{\nabla \mathbf{u}}$.

We now define a vector $\delta\ell^\perp$ normal to $\delta\ell$ with the same norm. This vector is simply $\delta\ell^\perp = (\delta\ell_y, -\delta\ell_x)$ and its dynamics obeys

$$\frac{d\delta\ell^\perp}{dt} = -(\overline{\nabla \mathbf{u}}^*) \delta\ell^\perp + (\nabla \cdot \mathbf{u}) \delta\ell^\perp, \quad (2.11)$$

where $\nabla \cdot \mathbf{u} = (\partial_x u, \partial_y v)$ is the flow divergence. For incompressible motions with $\nabla \cdot \mathbf{u} = 0$, we simply have $\dot{\delta\ell}^\perp = -(\overline{\nabla \mathbf{u}}^*) \delta\ell^\perp$.

The norm of $\delta\ell^\perp$ intensifies when the length $\delta\ell$ of the segment increases. In an incompressible flow this stretching of $\delta\ell$ implies that the lines parallel to the stripe get closer (as depicted by blue lines in figure 2). It leads to an intensification of the gradient of a passive substance in the direction normal to it, that is, in the direction of $\delta\ell^\perp$. For instance, if a blob with area $\delta\ell_0 s_0$ and concentration c elongates into a stripe of length $\delta\ell$

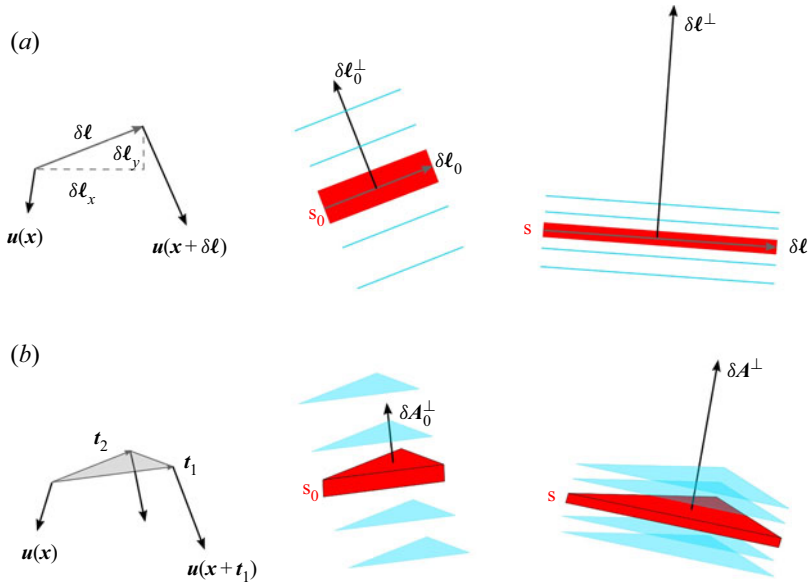


Figure 2. Schematic of the evolution of a segment (a) and a surface (b) elongated by a flow $u(x)$. In two dimensions a blob with area $s_0\delta\ell_0$ is elongated into a stripe of length $\delta\ell$ and transverse size s so that $s\delta\ell \sim s_0\delta\ell_0$. The iso-values of scalar denoted as blue lines are compressed. The concentration gradient across the stripe increases proportionally to $1/s$, i.e. to $\delta\ell$. The concentration gradient vector is thus proportional to $\delta\ell^\perp$. In three dimensions the same construction is valid for a blob of volume $s_0\delta A_0$ such that the concentration gradient is proportional to δA^\perp .

and transverse size s so that $\delta\ell \sim \delta\ell_0 s_0/s$, as in figure 2, the concentration gradient across the stripe c/s first increases proportionally to the norm $\delta\ell$ of the vector $\delta\ell^\perp$, before being smeared out by diffusion. It is therefore natural, as first underlined by Corrsin (1953) and later Brethouwer, Hunt & Nieuwstadt (2003), to find the operator $-\overline{\nabla u}^*$ instead of $\overline{\nabla u}$ in the evolution equation of scalar gradients (see also Batchelor & Townsend (1956) and Ertel (1942) in related contexts),

$$\frac{d \nabla c}{dt} = -\overline{\nabla u}^*(\nabla c) + D \nabla^2(\nabla c). \quad (2.12)$$

As also noted by Corrsin (1953), this equation differs from the vorticity equation since the scalar gradient is a lamellar vector (i.e. $\nabla \times (\nabla c) = 0$) whereas the vorticity is solenoidal (i.e. $\nabla \cdot \omega = 0$). In a Fourier decomposition of the scalar concentration field this operator also governs the wavevectors norm (see equation (2.5) in Kraichnan 1974).

2.2.2. Extension to three dimensions

Let us consider a surface element of area δA_i normal to the unit vector \mathbf{n}_i at a position x_i and at time t (see figure 2). We define, as above, the surface vector $\delta A_i = \delta A_i \mathbf{n}_i$, initially equal to δA_0 . The norm of δA_i is proportional to the surface area δA_i . Since δA_i is normal to the surface, it follows the same evolution as $\delta\ell$ in two dimensions that was governed by (2.11). Indeed, it can be shown by assuming that δA_i is the cross-product of two tangential

vectors $\mathbf{t}_1 \times \mathbf{t}_2$ that

$$\frac{d\delta\mathbf{A}_i}{dt} = \frac{d\mathbf{t}_1}{dt} \times \mathbf{t}_2 + \mathbf{t}_1 \times \frac{d\mathbf{t}_2}{dt} \quad (2.13)$$

$$= (\overline{\nabla}\mathbf{u} \mathbf{t}_1) \times \mathbf{t}_2 + \mathbf{t}_1 \times (\overline{\nabla}\mathbf{u} \mathbf{t}_2) \quad (2.14)$$

$$= -\overline{\nabla}\mathbf{u}^* (\mathbf{t}_1 \times \mathbf{t}_2) + (\nabla \cdot \mathbf{u})(\mathbf{t}_1 \times \mathbf{t}_2) \quad (2.15)$$

$$= -\overline{\nabla}\mathbf{u}^* \delta\mathbf{A}_i + (\nabla \cdot \mathbf{u}) \delta\mathbf{A}_i, \quad (2.16)$$

where $\overline{\nabla}\mathbf{u}^*(\mathbf{x}_i, t)$ is the transpose of the velocity gradient tensor $\overline{\nabla}\mathbf{u}(\mathbf{x}_i, t)$ such that

$$\overline{\nabla}\mathbf{u} = \begin{bmatrix} \partial_x u & \partial_y u & \partial_z u \\ \partial_x v & \partial_y v & \partial_z v \\ \partial_x w & \partial_y w & \partial_z w \end{bmatrix}, \text{ giving } \overline{\nabla}\mathbf{u}^* = \begin{bmatrix} \partial_x u & \partial_x v & \partial_x w \\ \partial_y u & \partial_y v & \partial_y w \\ \partial_z u & \partial_z v & \partial_z w \end{bmatrix}. \quad (2.17)$$

For an incompressible flow with $\nabla \cdot \mathbf{u} = 0$, the surface vector evolves according to the linear equation

$$\frac{d\delta\mathbf{A}_i}{dt} = -\overline{\nabla}\mathbf{u}^* \delta\mathbf{A}_i. \quad (2.18)$$

As classically done for the study of pair dispersion, it is convenient to define the tensor $\mathbf{L}_i(t)$ by

$$\frac{d\mathbf{L}_i}{dt} = -\overline{\nabla}\mathbf{u}^* \mathbf{L}_i, \quad \text{with } \mathbf{L}_i(t=0) = \mathbf{I}, \quad (2.19)$$

where $\overline{\nabla}\mathbf{u}^*$ is calculated at position $\mathbf{x}_i(t)$ and with \mathbf{I} the diagonal unit matrix. At time t , the surface vector is then equal to

$$\delta\mathbf{A}_i(t) = \mathbf{L}_i(t)\delta\mathbf{A}_0. \quad (2.20)$$

The same solution holds in two dimensions for $\delta\ell^\perp(t)$.

2.2.3. Ranz transform

The striation thickness s_i is explicit from (2.7) by replacing $\delta\mathbf{A}_i^2 = \delta\mathbf{A}_i^* \delta\mathbf{A}_i$ with its solution (2.20),

$$s_i = s_0(\mathbf{n}_0^* \mathbf{L}^* \mathbf{L} \mathbf{n}_0)^{-1/2}, \quad (2.21)$$

whereas the time τ_i is given explicitly by introducing this formula into (2.4),

$$\tau_i = \mathbf{n}_0^* \mathbf{T}_i \mathbf{n}_0, \quad (2.22)$$

where we have defined the operator

$$\mathbf{T}_i = \mathbf{I} + \frac{4D}{s_0^2} \int_0^t \mathbf{L}_i^* \mathbf{L}_i dt. \quad (2.23)$$

As before, the concentration profile across a diffuselet initially perpendicular to \mathbf{n}_0 is a Gaussian profile given by (2.6) with s_i and τ_i given above. These formulae are obviously also valid in two dimensions with \mathbf{n}_0 being the unit vector perpendicular to the filamentary strip element.

Consider the 2-D sine flow as an example. The result is exactly similar to the one plotted in figure 1(d) when taking initially the diffuselets along the filament of figure 1(c).

However, this method also works for independent diffuselets with arbitrary orientations θ_i , as shown in figure 1(e). Defining the normal vector $\mathbf{n}_i = (-\sin \theta_i, \cos \theta_i)$ leads to the position, orientation, diffusive thickness and maximal concentration of the diffuselet after 15 iterations, as plotted in figure 1(e).

The final result so obtained is exactly the same as that given by Balkovsky & Fouxon (1999) using the second momentum of scalar for an ellipsoidal blob with axes of initial length $2e^{\rho_{01}}$, $2e^{\rho_{02}}$ and $2e^{\rho_{03}}$. Assuming that the axis e^{ρ_3} is much smaller than the two other axes, i.e. that the blob is a surface element, they find that the diffusive length is equal to $2e^{\rho_3}$ with ρ_3 given in their formula (2.5), where $\tilde{\sigma}_{33}$ is the compression rate along the smallest axis ρ_3 . Although very different at first glance, their formula can be simplified into our formula by noting that $2e^{\rho_{03}} = s_0$ and that $\int \tilde{\sigma}_{33} dt = \log(s_i/s_0)$. From their result, the diffusive thickness is equal to

$$2e^{\rho_3} = s_i \sqrt{1 + \int_0^t \frac{4D}{s_i^2}}, \quad (2.24)$$

which is identical to our result $s_i \sqrt{\tau_i}$ (see also de Rivas & Villermaux 2016). The main problem in their derivation is that the compression rate $\tilde{\sigma}_{33}$ must be calculated in the local frame of reference aligned with the ellipsoid. Although theoretically possible, this rotation of the basis is difficult to do numerically. This is why our technique is simpler since the orientation of the surface is not required at each time.

It should be noted that the use of the tensors \mathbf{L}_i and \mathbf{T}_i is not required if each diffuselet is chosen with a unique initial orientation. Indeed, it would be possible to integrate (2.18) in time to get the surface vector δA_i from which s_i and τ_i can be obtained. This would require the storage of seven variables (for x_i , δA_i and τ_i) instead of 18 (for x_i , \mathbf{L}_i and the symmetric tensor τ_i). However, using the tensors \mathbf{L}_i and \mathbf{T}_i permits us to vary *a posteriori* the orientation of the diffuselet. This helps to converge the statistics when calculating the p.d.f. of the scalar, as will be shown in the next section.

2.3. Statistics over the initial orientation of the diffuselet

Several quantities have been extensively studied in the context of mixing. In the absence of diffusion (i.e. for $D = 0$), the stretching factor or the Lyapunov exponent are known to characterize the properties of the flow. Generally, it is the stretching factor between two points which is calculated from the eigenvalues of the tensor $\mathbf{L}_p^* \mathbf{L}_p$, where \mathbf{L}_p is the pair dispersion tensor solution of $d\mathbf{L}_p/dt = \overline{\nabla u} \mathbf{L}_p$. In our case we are more interested by the stretching factor of the surfaces since it corresponds to the compression factor of the striation thickness, which governs the diffusion problem. As shown above, the stretching factor $\rho = \delta A_i / \delta A_0$ of a diffuselet is simply given by

$$\rho = (\mathbf{n}_0^* \mathbf{L}_i^* \mathbf{L}_i \mathbf{n}_0)^{1/2}, \quad (2.25)$$

where \mathbf{n}_0 is the unit vector normal to the initial diffuselet. We now describe the 2-D and 3-D cases sequentially, in order to obtain concrete analytical formulae in each case.

2.3.1. Two-dimensional case

In two dimensions and for a given diffuselet i at time t , the tensor $\mathbf{L}_i^* \mathbf{L}_i$ is symmetric and its two eigenvalues are inverse because of the incompressibility. They are called μ_i and μ_i^{-1} with $\mu_i > 1$. On the basis of the tensor $\mathbf{L}_i^* \mathbf{L}_i$ the unit vector is taken as $\mathbf{n}_0 = (\cos \theta, \sin \theta)$,

The diffuselet concept for scalar mixing

with θ varying from 0 to $\pi/2$. The stretching factor $\rho_i = \delta\ell_i/\delta\ell_0$ of the diffuselet is given by

$$\rho_i^2 = \mu_i \cos^2 \theta + \mu_i^{-1} \sin^2 \theta. \quad (2.26)$$

The mean Lyapunov exponent $\bar{\lambda}_i = \langle \log \rho_i \rangle / t$ over all initial orientations can be calculated by averaging over θ ,

$$\bar{\lambda} = \frac{1}{t} \frac{1}{\pi/2} \int_{\theta=0}^{\pi/2} \frac{1}{2} \log(\mu_i \cos^2 \theta + \mu_i^{-1} \sin^2 \theta) d\theta. \quad (2.27)$$

The integral can be calculated analytically, which leads to a simple expression for the mean Lyapunov exponent of all diffuselets

$$\bar{\lambda} = \frac{\langle \log \rho \rangle}{t} = \frac{1}{Nt} \sum_{i=1}^N \log \left(\frac{1 + \mu_i}{2\sqrt{\mu_i}} \right). \quad (2.28)$$

Nevertheless, it is possible to get more information from the eigenvalues of the tensor \mathbf{L}_i . Indeed, the p.d.f. of the stretching factor for this diffuselet satisfies

$$P_i(\rho) d\rho = \frac{d\theta}{\pi/2}, \quad (2.29)$$

which can be written as $P_i(\rho) = 2/(\pi d\rho/d\theta)$. Calculating $d\rho/d\theta$ and using the fact that $\cos^2 \theta = (\rho^2 - \mu_i^{-1})/(\mu_i - \mu_i^{-1})$ and $\sin^2 \theta = (\mu_i - \rho^2)/(\mu_i - \mu_i^{-1})$ leads to

$$P_i(\rho) = \frac{2\rho}{\pi\sqrt{\mu_i - \rho^2}\sqrt{\rho^2 - \mu_i^{-1}}}, \quad (2.30)$$

with ρ varying between μ_i^{-1} and μ_i . Because the stretching factors often increase exponentially in time, it is more convenient to calculate the p.d.f. of $\log \rho$ using the fact that $P_i(\log \rho) = \rho P_i(\rho)$. This formula can then be averaged over the N diffuselets to get the statistics of the stretching factor,

$$P(\log \rho) = \frac{1}{N} \sum_{i=1}^N \frac{2\rho^2}{\pi\sqrt{\mu_i - \rho^2}\sqrt{\rho^2 - \mu_i^{-1}}}. \quad (2.31)$$

This p.d.f. of $\log \rho$ is plotted in [figure 3\(a\)](#) as red symbols for a 2-D sine flow. It is already well converged for only $N = 1000$ diffuselets homogeneously distributed for x and y in $[0; 1]$. This comes from the fact that each diffuselet incorporates all the orientations \mathbf{n}_0 at the same time thanks to the tensor \mathbf{L}_i . If the calculation was done for a single orientation (i.e. by solving an equation for $\delta\mathbf{A}_i$ rather than for \mathbf{L}_i), the p.d.f. would be obtained as the histogram of stretching factors ρ_i . This is what is plotted in [figure 3\(a\)](#) as blue symbols. It is clear that the number of diffuselets is not sufficient for the convergence of the p.d.f. It indicates that the use of the tensor \mathbf{L}_i is extremely efficient despite a slightly larger memory usage. The parabolic shape of the p.d.f. will be studied in detail in § 3 and compared with theoretical predictions.

The strength of the diffuselet method is that the scalar field around each tracer is known quantitatively. The variance of concentration can be calculated analytically for each diffuselet and then averaged when the initial orientation is varied. As a first step,

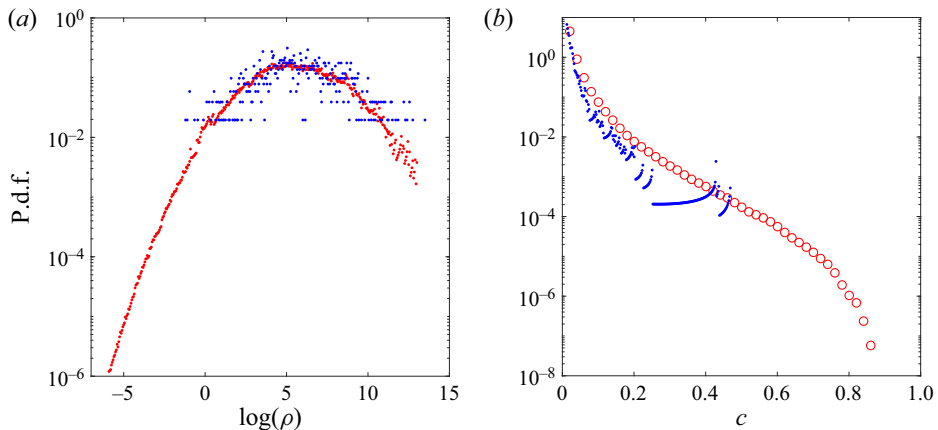


Figure 3. Probability distribution function of the stretching rate (a) and scalar concentration (b) obtained for 1000 diffuselets in a 2-D sine flow after 50 iterations. The blue symbols correspond to a single initial orientation \mathbf{n}_0 along the y axis whereas red symbols correspond to an ensemble average with \mathbf{n}_0 taking all orientations, as given by (2.31) and (2.38).

it is interesting to model the Gaussian transverse profile by a top-hat profile with maximal concentration $C_i = 1/\sqrt{\tau_i}$, diffusive thickness $s_i\sqrt{\tau_i}$ and length $\delta\ell_0 s_0/s_i$. Thus, this rectangular diffuselet has an area $\delta\ell_0 s_0\sqrt{\tau_i}$ that is equal to $\delta\ell_0 s_0/C_i$. We can check here that the total quantity of scalar ($C_i \times$ initial area) is conserved with time. Each diffuselet has a variance $\int c^2(x, y) dx dy$ equal to C_i^2 multiplied by its area. This variance is thus simply equal to $C_i \delta\ell_0 s_0$. The maximal concentration $C_i = 1/\sqrt{\tau_i}$ can be written using (2.22),

$$C_i = (\eta_i \cos^2 \theta + \eta'_i \sin^2 \theta)^{-1/2}, \quad (2.32)$$

where $\eta_i > \eta'_i$ are the two positive eigenvalues of the symmetric tensor \mathbf{T}_i (by writing $\mathbf{n}_0 = (\cos \theta, \sin \theta)$ on the basis of the eigenvectors). The mean variance is thus equal to

$$\langle c^2 \rangle_{top-hat} = \frac{\delta\ell_0 s_0}{\pi/2} \int_{\theta=0}^{\pi/2} \frac{d\theta}{[\eta_i \cos^2(\theta) + \eta'_i \sin^2(\theta)]^{1/2}}. \quad (2.33)$$

The integral can be computed analytically leading to a simple formula for the variance,

$$\langle c^2 \rangle_{top-hat} = \frac{2\delta\ell_0 s_0 K(1 - \eta_i/\eta'_i)}{\pi \sqrt{\eta'_i}}, \quad (2.34)$$

with K the complete elliptic integral of the first kind.

The variance $\int c^2(x, y) dx dy$ for a Gaussian profile as in (2.6) can then be calculated easily since for each θ it is equal to the variance of the top-hat profile multiplied by $\sqrt{\pi/2}$. Summing over all diffuselets, the total variance reads

$$\langle c^2 \rangle = \frac{\sqrt{2}\delta\ell_0 s_0}{\sqrt{\pi}} \sum_{i=1}^N \frac{K(1 - \eta_i/\eta'_i)}{\sqrt{\eta'_i}}. \quad (2.35)$$

For each diffuselet, the p.d.f. of concentration can also be calculated when varying the initial orientation of the diffuselet. As a first step, the top-hat profile is considered such

that the contribution of each diffuselet to the p.d.f. at $C = C_i$ is proportional to its area $\delta\ell_0 s_0 / C_i$. The p.d.f. of maximal concentration thus contains two peaks at $C = 0$ and $C = C_i$ for a single diffuselet with a single initial orientation. However, C_i depends on the initial orientation according to (2.32). For each diffuselet, the p.d.f. of maximal concentration is given by

$$Q_i(C) dC = \frac{s_0 \delta \ell_0}{C} \frac{d\theta}{\pi/2}, \quad (2.36)$$

with θ varying uniformly from 0 to $\pi/2$. Indeed, the initial orientation of the diffuselets is *a priori* random, with no privileged direction. This does not mean that the diffuselets will not align in the flow, they will in, for instance, the presence of a sustained, persistent shear in the flow, or can remain randomly oriented if the flow is itself random.

Using the fact that $\cos^2 \theta = (C^{-2} - \eta'_i)/(\eta_i - \eta'_i)$ and $\sin^2 \theta = (\eta_i - C^{-2})/(\eta_i - \eta'_i)$, we can calculate $dC/d\theta = C^3 \sqrt{C^{-2} - \eta'_i} \sqrt{\eta_i - C^{-2}}$. The p.d.f. of maximal concentration reads

$$Q_i(C) = \frac{2\delta\ell_0 s_0}{\pi C^4 \sqrt{C^{-2} - \eta'_i} \sqrt{\eta_i - C^{-2}}}, \quad (2.37)$$

with C varying from $1/\sqrt{\eta_i}$ to $1/\sqrt{\eta'_i}$.

Replacing the top-hat profile by a Gaussian profile is easily done by convolution with the p.d.f. of a Gaussian profile with maximal concentration C (see, e.g. Villermaux 2019), $1/(c\sqrt{\log(C/c)})$. The p.d.f. of concentration is thus equal to

$$P_i(c) = \frac{2\delta\ell_0 s_0}{\pi c} \int_{C=1/\sqrt{\eta_i}}^{C=1/\sqrt{\eta'_i}} \frac{dC}{C^4 \sqrt{C^{-2} - \eta'_i} \sqrt{\eta_i - C^{-2}} \sqrt{\log(C/c)}}. \quad (2.38)$$

This formula can then be averaged over all diffuselets to get the total p.d.f. of concentration $P(c) = \sum P_i(c)$. It is plotted in figure 3(b) as red symbols. It is converged over eight decades although only 1000 diffuselets are used. As before, this convergence is not possible without the use of the tensor T_i . Indeed, when fixing the initial orientation of the diffuselet along the x axis, the p.d.f. (plotted as blue symbols) in figure 3(b) is only converged over three decades from 10^{-2} to 10. This clearly highlights the efficiency of the tensor calculation.

It should be noted that this p.d.f. is normalised such that its first moment $\int c P_i(c) dc$ is equal to the total quantity of scalar of the i th diffuselet $\delta\ell_0 s_0 / \sqrt{\pi}$. The first moment of the maximum concentration $\int Q_i(C) dC$ is also equal to the total quantity of scalar $\delta\ell_0 s_0$ for a top-hat profile. This choice of normalisation is not classical but it prevents the well-known technically annoying, although physically harmless, ambiguity caused by the divergence of $P_i(c)$ in unbounded domains (Villermaux 2019). Indeed, the Gaussian profile of concentration induces a singularity as $1/c$ for vanishing c that prevents a normalisation satisfying $\int P_i(c) dc = 1$. This choice also allows us to recover the variance of concentration $\langle c^2 \rangle$ found in (2.35) as the second moment of the p.d.f. of concentration $\int c^2 P(c) dc$.

2.3.2. Three-dimensional case

The same formulae are provided in three dimensions, although they are slightly more complex. The p.d.f. of surface stretching is still governed by the eigenvalues of the

symmetric tensor $\mathbf{L}_i^* \mathbf{L}_i$. They are positive and can be ordered as $\mu_i > \mu'_i > \mu''_i$. We can choose a basis aligned with the eigenvectors, such that the tensor $\mathbf{L}_i^* \mathbf{L}_i$ is diagonal with its diagonal being (μ''_i, μ'_i, μ_i) . We choose the initial normal vector of the diffuselet to be

$$\mathbf{n}_0 = (\sin \theta \cos \phi, \sin \theta \sin \phi, \cos \theta). \quad (2.39)$$

Using (2.25), the surface stretching $\rho_i = \delta A_i / \delta A_0$ is thus equal to

$$\rho_i = [\sin^2 \theta (\mu''_i \cos^2 \phi + \mu'_i \sin^2 \phi) + \mu_i \cos^2 \theta]^{1/2}. \quad (2.40)$$

The mean Lyapunov exponent $\langle \log \rho \rangle / t$ can thus be obtained easily by averaging over θ and ϕ and over all (initially randomly oriented) diffuselets,

$$\bar{\lambda} = \frac{1}{N} \sum_{i=1}^N \int_{\phi=0}^{\pi/2} \int_{\theta=0}^{\pi/2} \frac{\log(\rho_i)}{t} \frac{\sin \theta \, d\theta \, d\phi}{\pi/2}, \quad (2.41)$$

where ρ_i is given by (2.40). This simple formula gives the mean Lyapunov exponent of small surface elements with a random initial position and orientation.

As in two dimensions, it is possible to get more information from the eigenvalues of the tensor \mathbf{L}_i . Indeed, the p.d.f. of stretching factor ρ is given by

$$P_i(\rho) \, d\rho = \frac{\sin \theta \, d\theta \, d\phi}{\pi/2}, \quad (2.42)$$

with ϕ varying from 0 to $\pi/2$ and θ varying from 0 to $\pi/2$ due to the symmetry of ρ across the equatorial plane and the symmetry of ρ when ϕ is changed in $-\phi$ or in $\phi + \pi$. In these conditions, the p.d.f. of ρ is simply

$$P_i(\rho) = \int_{\theta=0}^{\pi/2} \frac{2 \sin \theta \, d\theta}{\pi \frac{\partial \rho}{\partial \phi}}, \quad (2.43)$$

with the denominator computed as

$$\frac{\partial \rho}{\partial \phi} = \frac{1}{\rho} [\sin^2 \theta (\mu_i - \mu''_i) - (\mu_i - \rho^2)]^{1/2} [(\mu_i - \rho^2) - \sin^2 \theta (\mu_i - \mu'_i)]^{1/2}, \quad (2.44)$$

which leads, with the change of variable $x = \sin^2 \theta$, to

$$P_i(\rho) = \frac{\rho}{\pi \sqrt{\mu_i - \mu''_i} \sqrt{\mu_i - \mu'_i}} \int_{x=x_1}^{\min(1, x_2)} \frac{dx}{\sqrt{1-x} \sqrt{x-x_1} \sqrt{x_2-x}}, \quad (2.45)$$

with $x_1 = (\mu_i - \rho^2)/(\mu_i - \mu''_i)$ and $x_2 = (\mu_i - \rho^2)/(\mu_i - \mu'_i)$. The numerical integration becomes difficult when ρ^2 is close to μ'_i because of a logarithmic divergence. It may be removed by doing the change of variable $x = (x_1 + x_2)/2 + x'(x_2 - x_1)/2$ if $\rho^2 > \mu'_i$ and the change of variable $x = (x_1 + 1)/2 + x'(1 - x_1)/2$ if $\rho^2 < \mu'_i$. This leads to the general

formulae

$$P_i(\rho) = \frac{\rho}{\pi\sqrt{\mu_i - \rho^2}\sqrt{\mu'_i - \mu''_i}} F\left[\frac{2(\rho^2 - \mu'_i)(\mu_i - \mu''_i)}{(\mu_i - \rho^2)(\mu'_i - \mu''_i)}\right] \quad \text{for } \mu'_i < \rho^2 < \mu_i \quad (2.46)$$

and

$$P_i(\rho) = \frac{\rho}{\pi\sqrt{\mu_i - \mu'_i}\sqrt{\rho^2 - \mu''_i}} F\left[\frac{2(\mu'_i - \rho^2)(\mu_i - \mu''_i)}{(\rho^2 - \mu''_i)(\mu_i - \mu'_i)}\right] \quad \text{for } \mu''_i < \rho^2 < \mu'_i, \quad (2.47)$$

where the function F is defined as

$$F(a) = \int_{-1}^1 \frac{\sqrt{2} dx}{\sqrt{1-x^2}\sqrt{1+a-x}} = \sqrt{\frac{8}{a}} K\left(-\frac{2}{a}\right) + \log\left(\frac{4+a+\sqrt{16+8a}}{(\sqrt{2}+\sqrt{2+a})^2}\right), \quad (2.48)$$

with K the complete elliptic integral of the first kind. This function diverges as $-\log a$ when a tends to 0 and is thus hardly computed using this formula. It can be replaced by adding and removing $\sqrt{1+x}$ to the numerator, leading to an approximate (within 1 %) formula

$$F(a) \approx \log\left|\left(\frac{4}{a} + 1\right) + \sqrt{\left(\frac{4}{a} + 1\right)^2 - 1}\right| - \frac{1.60}{\sqrt{a+1.40}} \quad (2.49)$$

that is computed 10 000 times faster than with the exact formula. These formulae can then be averaged to get the total p.d.f. $P(\rho) = \sum P_i(\rho)/N$ and the total p.d.f. $P(\log \rho) = \sum \rho P_i(\rho)/N$.

As in two dimensions, the concentration variance can be calculated analytically. As a first step, the Gaussian transverse profile is modelled by a top-hat profile with maximal concentration $C_i = 1/\sqrt{\tau_i}$, diffusive thickness $s_i\sqrt{\tau_i}$ and surface $\delta A_0 s_0/s_i$. This diffuselet is rectangular parallelepiped with volume $\delta A_0 s_0 \sqrt{\tau_i} = \delta A_0 s_0/C_i$. Once again, the total quantity of scalar is conserved. The variance $\int c^2(x, y, z) dx dy dz$ is equal to C_i^2 times its volume with $C_i = 1/\sqrt{\tau_i}$ given by (2.22),

$$C_i = [\sin^2 \theta (\eta''_i \cos^2 \phi + \eta'_i \sin^2 \phi) + \eta_i \cos^2 \theta]^{-1/2}, \quad (2.50)$$

where $\eta_i > \eta'_i > \eta''_i$ are the three positive eigenvalues of the symmetric tensor \mathbf{T}_i and where the initial orientation is taken equal to

$$\mathbf{n}_0 = (\sin \theta \cos \phi, \sin \theta \sin \phi, \cos \theta) \quad (2.51)$$

on the basis of the eigenvectors. Averaging over all uniformly distributed initial orientations, we find that

$$\langle c^2 \rangle_{top-hat} = \int_{\phi=0}^{\pi/2} \int_{\theta=0}^{\pi/2} \frac{\delta A_0 s_0}{[\sin^2 \theta (\eta''_i \cos^2 \phi + \eta'_i \sin^2 \phi) + \eta_i \cos^2 \theta]^{-1/2}} \frac{\sin \theta d\theta d\phi}{\pi/2}. \quad (2.52)$$

The integral over θ can be calculated analytically. The total variance for a Gaussian profile is then obtained by multiplying by $\sqrt{\pi/2}$ and by summing over i ,

$$\langle c^2 \rangle = \frac{\sqrt{2} \delta A_0 s_0}{\sqrt{\pi}} \sum_{i=1}^N \int_0^{\pi/2} \frac{\operatorname{asinh}(\sqrt{\eta_i/G_i(\phi)-1}) d\phi}{\sqrt{\eta_i - G_i(\phi)}}, \quad (2.53)$$

with $G_i(\phi) = \eta''_i \cos^2(\phi) + \eta'_i \sin^2(\phi)$. This formula is extremely useful to get a quick characterization of the mixing rate of the flow. Indeed, it is easily computed numerically by advecting tracers in the flow and calculating the tensors \mathbf{L}_i from (2.19) and \mathbf{T}_i from (2.23), leading immediately to the eigenvalues η_i , η'_i and η''_i .

As in two dimensions, the final step consists in calculating the p.d.f. of concentration analytically. For a top-hat profile, each diffuselet of volume $\delta A_0 s_0 / C_i$ contributes to the p.d.f. at $C = C_i$ with a weight $\delta A_0 s_0 / C_i$. When varying the initial orientation of the diffuselet, the p.d.f. of maximal concentration is given by

$$Q_i(C) dC = \frac{\delta A_0 s_0}{C} \frac{\sin \theta d\theta d\phi}{\pi/2}, \quad (2.54)$$

with ϕ varying from 0 to $\pi/2$ and θ varying from 0 to $\pi/2$. It can be written as

$$Q_i(C) = \frac{\delta A_0 s_0}{\pi C} \int_{\theta=0}^{\pi/2} \frac{2 \sin \theta d\theta}{\frac{\partial C}{\partial \phi}}. \quad (2.55)$$

Inside the integral, the denominator can be calculated as

$$\frac{\partial C}{\partial \phi} = C^3 [\sin^2 \theta (\eta_i - \eta''_i) - (\eta_i - C^{-2})]^{1/2} [(\eta_i - C^{-2}) - \sin^2 \theta (\eta_i - \eta'_i)]^{1/2}. \quad (2.56)$$

Doing the change of variable $x = \sin^2 \theta$ leads to the formula

$$Q_i(C) = \frac{2 \delta A_0 s_0}{\pi C^4 \sqrt{\eta_i - \eta''_i} \sqrt{\eta_i - \eta'_i}} \int_{x=x_1}^{\min(1, x_2)} \frac{dx}{\sqrt{1-x} \sqrt{x-x_1} \sqrt{x_2-x}}, \quad (2.57)$$

with $x_1 = (\eta_i - C^{-2}) / (\eta_i - \eta''_i)$ and $x_2 = (\eta_i - C^{-2}) / (\eta_i - \eta'_i)$. Doing the final change of variable $x = (x_1 + x_2)/2 + x'(x_2 - x_1)/2$ if $C^{-2} > \mu'_i$ and the change of variable $x = (x_1 + 1)/2 + x'(1 - x_1)/2$ if $C^{-2} < \mu'_i$. This leads to the general formulae

$$Q_i(C) = \frac{\delta A_0 s_0}{\pi C^4 \sqrt{\eta_i - \eta'_i} \sqrt{C^{-2} - \eta''_i}} F \left[\frac{2(\eta'_i - C^{-2})(\eta_i - \eta''_i)}{(C^{-2} - \eta''_i)(\eta_i - \eta'_i)} \right] \quad \text{for } \eta''_i < C^{-2} < \eta'_i \\ (2.58)$$

and

$$Q_i(C) = \frac{\delta A_0 s_0}{\pi C^4 \sqrt{\eta_i - C^{-2}} \sqrt{\eta'_i - \eta''_i}} F \left[\frac{2(C^{-2} - \eta'_i)(\eta_i - \eta''_i)}{(\eta_i - C^{-2})(\eta'_i - \eta''_i)} \right] \quad \text{for } \eta'_i < C^{-2} < \eta_i, \\ (2.59)$$

where the function F is defined by (2.48).

Replacing the top-hat profile by a Gaussian profile is easily done by convolution with the p.d.f. of a Gaussian profile $1/(c\sqrt{\log(C/c)})$. This formula can then be summed over all diffuselets to get the total p.d.f. of concentration,

$$P(c) = \int_{C=c}^{C=1} \frac{\sum_{i=1}^N Q_i(C)}{c\sqrt{\log(C/c)}} dC. \quad (2.60)$$

As in two dimensions, this p.d.f. is normalized such that its first moment $\int c P(c) dc$ is equal to the total quantity of scalar of all diffuselets $\sum \delta A_0 s_0 / \sqrt{\pi}$. We also recover the fact that the variance of concentration $\langle c^2 \rangle$, previously calculated in (2.53), is equal to $\int c^2 P(c) dc$ but also to $\sqrt{\pi/2} \int C^2 Q(C) dC$.

3. Two-dimensional sine flow

3.1. Analytical formulae for the trajectories and the tensors of the diffuselets

We apply the technique developed above to the case of a two-dimensional random sine flow with a wavelength equal to 1. It is defined for the n th time interval by

$$\text{Step 1: } \mathbf{u} = U \begin{bmatrix} 0 \\ \sin[2\pi x + \chi_1(n)] \end{bmatrix} \quad \text{if } t \in \left[n; n + \frac{1}{2}\right], \quad (3.1)$$

$$\text{Step 2: } \mathbf{u} = U \begin{bmatrix} \sin[2\pi y + \chi_2(n)] \\ 0 \end{bmatrix} \quad \text{if } t \in \left[n + \frac{1}{2}; n + 1\right]. \quad (3.2)$$

Here, U corresponds to the amplitude of the flow, χ_1 and χ_2 are random phases between 0 and 2π (see [table 1](#) for the first ten values) and n is an integer. The trajectory \mathbf{x}_i of a tracer initially at (x_0, y_0) can be integrated analytically during each time interval. For example, for the n th time interval, x_i is constant during step 1 (i.e. for $t \in [n; n + 1/2]$) because the x velocity vanishes; $x_i(t)$ is thus equal to $x_i(n)$ such that the y velocity is constant. The y position is thus linear in time $y_i(t) = y_i(n) + U(t - n) \sin[2\pi x_i(n) + \chi_1(n)]$. Similarly, y_i is constant during step 2 such that its x velocity is constant and $x_i(t) = x_i(n) + U(t - n - 1/2) \sin[2\pi y_i(n + 1/2) + \chi_2(n)]$, where we have used the fact that $x_i(n + 1/2) = x_i(n)$. It should be noted that y_i is constant during step 2 such that $y_i(n + 1/2) = y_i(n + 1)$. To conclude, the positions at time $t = n$ are simply obtained by applying

$$y_i(n + 1) = y_i(n) + \frac{U}{2} \sin[2\pi x_i(n) + \chi_1(n)], \quad (3.3)$$

$$x_i(n + 1) = x_i(n) + \frac{U}{2} \sin[2\pi y_i(n + 1) + \chi_2(n)], \quad (3.4)$$

for $n = 0, 1, 2, \dots, T_{max}$.

We now calculate the tensors \mathbf{L}_i and \mathbf{T}_i analytically. We first focus on the first step. During step 1, x_i is constant such that the velocity gradient is constant and equal to

$$\overline{\nabla} \mathbf{u} = \begin{bmatrix} 0 & 0 \\ \gamma & 0 \end{bmatrix}, \quad \text{with } \gamma = 2\pi U \cos[2\pi x_i(n) + \chi_1(n)]. \quad (3.5)$$

The tensor $\mathbf{L}_i(t)$ is given by an exponential matrix $\exp[-\int \overline{\nabla} \mathbf{u}^* dt] \mathbf{L}_i(n)$ that is simply equal to $[\mathbf{I} - (t - n) \overline{\nabla} \mathbf{u}^*] \mathbf{L}_i(n)$ since $\overline{\nabla} \mathbf{u}^{*2}$ vanishes (using the Taylor expansion of the exponential). During step 1, the tensor reads

$$\mathbf{L}_i(t) = \begin{bmatrix} 1 & -\gamma(t - n) \\ 0 & 1 \end{bmatrix} \mathbf{L}_i(n), \quad \text{with } \gamma = 2\pi U \cos[2\pi x_i(n) + \chi_1(n)]. \quad (3.6)$$

It is then easy to compute the tensor \mathbf{T}_i from [\(2.23\)](#). At time $t = n + 1/2$ it reads

$$\mathbf{T}_i \left(n + \frac{1}{2} \right) = \mathbf{T}_i(n) + \frac{4D}{s_0^2} \mathbf{L}_i^*(n) \begin{bmatrix} \frac{1}{2} & -\frac{\gamma}{8} \\ -\frac{\gamma}{8} & \frac{1}{2} + \frac{\gamma^2}{24} \end{bmatrix} \mathbf{L}_i(n). \quad (3.7)$$

For the second step, the technique is similar although the formulae are slightly different. We find that

$$\mathbf{L}_i(t) = \begin{bmatrix} 1 & 0 \\ -\gamma \left(t - n - \frac{1}{2} \right) & 1 \end{bmatrix} \mathbf{L}_i \left(n + \frac{1}{2} \right), \quad (3.8)$$

with $\gamma = 2\pi U \cos[2\pi y_i(n+1) + \chi_2(n)]$ and

$$\mathbf{T}_i(n+1) = \mathbf{T}_i\left(n + \frac{1}{2}\right) + \frac{4D}{s_0^2} \mathbf{L}_i^* \left(n + \frac{1}{2}\right) \begin{bmatrix} \frac{1}{2} + \frac{\gamma^2}{24} & -\frac{\gamma}{8} \\ -\frac{\gamma}{8} & \frac{1}{2} \end{bmatrix} \mathbf{L}_i\left(n + \frac{1}{2}\right). \quad (3.9)$$

To conclude, the tensors can be calculated from time n to time $n+1$ by applying successively (3.6) at time $t = n + 1/2$, (3.7), (3.8) at time $t = n+1$ and (3.9). The initial values are simply $\mathbf{L}(0) = \mathbf{T}(0) = \mathbf{I}$. This procedure is extremely fast because there is no temporal integration of the Lagrangian trajectories in each time interval as used previously by Meunier & Villermaux (2010). It is thus possible to obtain the trajectories of 1000 diffuselets over 15 periods in only 0.8 s whereas it takes 192 s using a temporal integration in each time interval. This central processing unit (CPU) time is four orders of magnitude faster than that for a DNS. It took a few hours to get a DNS with 8192^2 Fourier modes despite its acceleration due to the property of the sine flow (see Appendix A). This theoretical implementation will be used in the following with a number of diffusers fixed to $N = 10^4$ for a good convergence (although convergence is correct for $N = 10^3$, as shown in figure 3).

3.2. Probability distribution function of stretching

As shown previously, the stretching factor $\rho = \delta\ell_i/\delta\ell_0$ for each diffuselet is simply given by the square root of $\mathbf{n}_0^* \mathbf{L}_i^* \mathbf{L}_i \mathbf{n}_0$. When averaging over all initial orientations \mathbf{n}_0 and all diffuselets, the p.d.f. of stretching factors is given in two dimensions by (2.31), where μ_i is the maximal eigenvalue of $\mathbf{L}_i^* \mathbf{L}_i$. This p.d.f. is plotted as dotted symbols in figure 4 at different times for a small velocity $U = 0.3$. After half a period, the p.d.f. has a cusp around 0. This singularity is due to the diffuselets that have not been stretched (whatever their initial orientation) since they are at a position where the shear $\gamma = \partial v/\partial x$ vanishes. After one period, the probability that a diffuselet has experienced no shear at the first and at the second half-period is small such that this singularity has disappeared (green symbols). As time evolves, the p.d.f. becomes more rounded. At late times the p.d.f.s are parabolic with a maximum located at a position increasing linearly in time. It indicates that the mean Lyapunov exponent

$$\bar{\lambda} = \langle \log \rho / t \rangle \quad (3.10)$$

is constant in time as classically obtained for chaotic flows. The variance of these distributions

$$V = \langle (\log \rho - \bar{\lambda}t)^2 \rangle \quad (3.11)$$

also increases linearly in time. This can be understood by decomposing the n periods into $2n$ independent stretching processes with the same mean stretching factor and the same variance. Here $\log \rho$ is obtained as the sum of $2n$ random processes, such that its average and its variance increase linearly in time due to the central limit theorem.

Interestingly, the average and the variance can be calculated analytically at $t = 1/2$ by doing an ensemble average over all diffuselets. Indeed, the tensor

$$\mathbf{L}^* \mathbf{L} = \begin{bmatrix} 1 & -\frac{\gamma}{2} \\ -\frac{\gamma}{2} & 1 + \frac{\gamma^2}{4} \end{bmatrix} \quad (3.12)$$

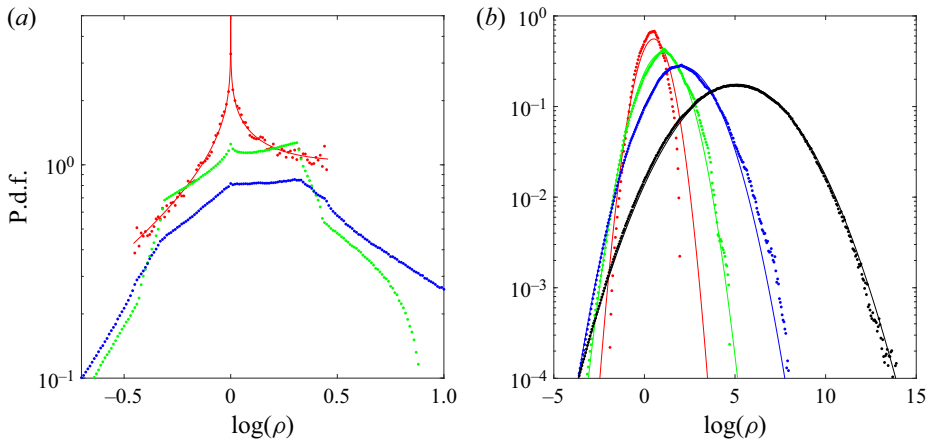


Figure 4. Probability distribution function of the stretching rate for $U = 0.3$. In (a) times are equal to $t = 0.5$ (red), $t = 1$ (green) and $t = 2$ (blue). In (b) times are equal to $t = 5$ (red), $t = 10$ (green), $t = 20$ (blue) and $t = 50$ (black). Symbols correspond to the diffuselet method given by (2.31). The solid lines correspond to the exact calculation (3.16) at $t = 0.5$ and to the normal law (3.19) at late times with the mean Lyapunov exponent and the variance given analytically by (3.17) and (3.18).

has a maximal eigenvalue

$$\mu_i = 1 + \frac{\gamma^2}{8} \left(1 + \sqrt{1 + 16\gamma^{-2}} \right), \quad \text{with } \gamma = 2\pi U \cos[2\pi x_i(0) + \chi_1(0)]. \quad (3.13)$$

By varying the position of the diffuselet $x_i(0)$ from $-\chi_1(0)/(2\pi)$ to $1/2 - \chi_1(0)/(2\pi)$, we find that

$$P(\mu_i) = \frac{|dx_i/d\mu_i|}{1/2}. \quad (3.14)$$

Using the fact that $x_i = \arccos[(\mu_i - 1)/(\pi\sqrt{\mu_i})]/(2\pi)$, the p.d.f. reads

$$P(\mu_i) = \frac{1 + \mu_i^{-1}}{\pi\sqrt{\pi^2 U^2 \mu_i - (\mu_i - 1)^2} \sqrt{\mu_i - \rho^2} \sqrt{\rho^2 - \mu_i^{-1}}}. \quad (3.15)$$

Replacing in (2.31) the discrete sum over the N diffusers by $\int P(\mu_i) d\mu_i$, we find the p.d.f. of the stretching factor

$$P_{1/2}(\log \rho) = \int_{\mu_i=\rho^2}^{\mu_i=\mu_M} \frac{2(1 + \mu_i^{-1})\rho^2 d\mu_i}{\pi^2 \sqrt{\pi^2 U^2 \mu_i - (\mu_i - 1)^2} \sqrt{\mu_i - \rho^2} \sqrt{\rho^2 - \mu_i^{-1}}}, \quad (3.16)$$

with $\mu_M = 1 + \pi^2 U^2 / 2 + \sqrt{\pi^4 U^4 / 4 + \pi^2 U^2}$. This analytical prediction at time $t = 1/2$ is plotted in figure 4(a) as a red line for $U = 0.3$. There is an excellent agreement with the numerical p.d.f.s plotted as red dots. From this analytical p.d.f. it is possible to calculate numerically the mean Lyapunov exponent from the first moment of $P_{1/2}(\log \rho)$. However, it is easier to use the general formula (2.28) for the Lyapunov exponent and to replace the

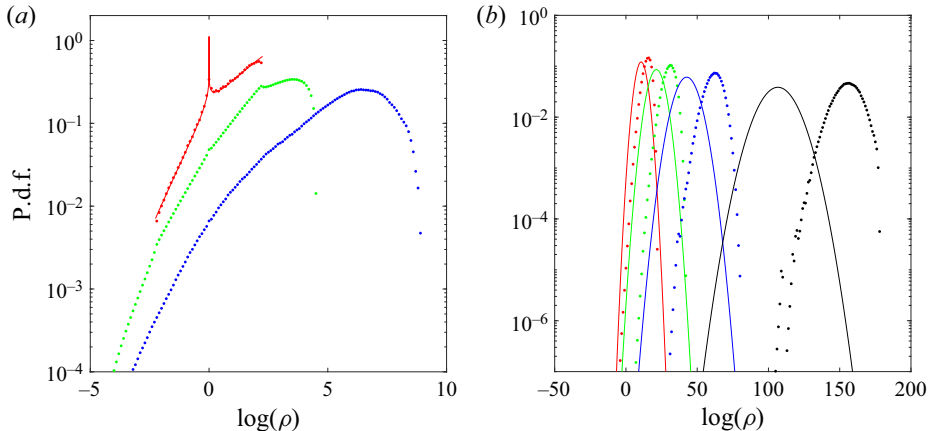


Figure 5. Probability distribution function of the stretching rate for $U = 3$. In (a) times are equal to $t = 0.5$ (red), $t = 1$ (green) and $t = 2$ (blue). In (b) times are equal to $t = 5$ (red), $t = 10$ (green), $t = 20$ (blue) and $t = 50$ (black). Symbols correspond to the diffuselet method given by (2.31). The solid lines correspond to the exact calculation (3.16) at $t = 0.5$ and to the normal law (3.19) at late times with the mean Lyapunov exponent and the variance given analytically by (3.17) and (3.18).

discrete sum by $\int P(\mu_i) d\mu_i$. It leads to a simple integral for the mean Lyapunov exponent,

$$\bar{\lambda}_{th} = \int_1^{\mu_M} \log \left(\frac{1 + \mu_i}{2\sqrt{\mu_i}} \right) \frac{2(1 + \mu_i^{-1})}{\pi\sqrt{\pi^2 U^2 \mu_i - (\mu_i - 1)^2}} d\mu_i. \quad (3.17)$$

Similarly, the variance of the distribution can be calculated as

$$V_{1/2} = \int_{\theta=0}^{\pi/2} \int_{\mu_i=1}^{\mu_M} \frac{\log^2(\mu_i \cos^2 \theta + \mu_i^{-1} \sin^2 \theta)(1 + \mu_i^{-1})}{4\pi\sqrt{\pi^2 U^2 \mu_i - (\mu_i - 1)^2}} d\mu_i - \frac{\bar{\lambda}_{th}^2}{4} \quad (3.18)$$

at time $t = 1/2$. These theoretical results can then be used to infer the p.d.f. of stretching rates at late times. After n periods, if the $2n$ stretching steps are independent random processes, the p.d.f. of $\log \rho$ must be, according to the central limit theorem, a normal law (see, e.g. equation (2.7) of Balkovsky & Fouixon 1999),

$$P_{th}(\log \rho) = \frac{1}{\sqrt{2\pi V_{th}(t)}} \exp \left[-\frac{(\log \rho - \bar{\lambda}_{th}t)^2}{2V_{th}(t)} \right], \quad \text{with } V_{th}(t) = \frac{t}{1/2} V_{1/2}. \quad (3.19)$$

This prediction is plotted as solid lines in figure 4 at late times. There is an excellent agreement with the numerical results for this small velocity amplitude $U = 0.3$. The position and width of the parabola are exactly similar between the numerics and the theory. However, when the amplitude of the velocity is increased to $U = 3$, figure 5 shows that there is a clear discrepancy by approximately 30 % on the position of the parabola at late times although the prediction is correct for $t = 1/2$. It indicates that the Lyapunov exponent obtained at $t = 1/2$ is smaller than that obtained at late times. This can be explained by the fact that the stretching steps are not independent random processes for this large velocity amplitude.

In order to analyse this discrepancy, the mean Lyapunov exponent is plotted in blue as a function of U in figure 6. The Lyapunov exponent increases quadratically for small velocity U and tends to saturate for a large velocity amplitude. For a small velocity amplitude U ,

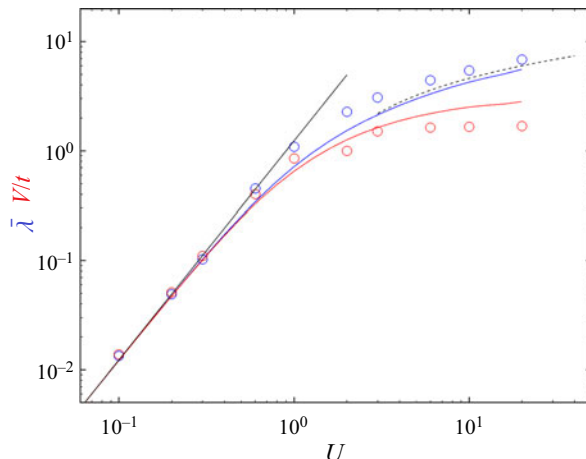


Figure 6. Mean Lyapunov exponent $\bar{\lambda} = \langle \log \rho \rangle / t$ (blue) and variance $V = \langle (\log \rho - \bar{\lambda}t)^2 \rangle$ (red) as a function of the velocity of the sine flow U . Solid lines correspond to the theoretical predictions calculated at $t = 0.5$ using (3.17) and (3.18). Numerical results averaged between $t = 20$ and $t = 50$ are plotted as symbols. Kraichnan's theoretical prediction (3.22) for a flow decorrelated in time is plotted as a black solid line. The Lyapunov exponent for large velocity amplitude (3.20) is plotted as a black dashed line.

there is an excellent agreement between the numerical values (plotted as blue symbols) and the theoretical values (plotted as a blue line). It means that the assumption of random independent stretching steps is correct. For a velocity amplitude of order 1, the Lyapunov exponent is larger by approximately 30 % in the numerics than in the theory, as noticed in the previous figure for $U = 3$. This is possibly due to the fact that at $t = 1/2$ the diffuselets are oriented along the y axis (whatever their initial orientation), which is optimal for the next step. They are more stretched by the shear in the second step than if they had a random orientation at $t = 1/2$ (as assumed in the theory). However, this effect seems to be rather limited: at a large velocity amplitude, the agreement between the numerics and the theory is again very good. This is because the stretching of the diffuselet at late times is independent of its initial orientation since it will be aligned with the direction of the shear.

It is commonly assumed that the diffuselets are aligned with the direction of maximum stretching rate at late times. Under this alignment assumption, the mean Lyapunov exponent $\bar{\lambda}$ must be equal to the spatial average of the positive stretching rate (Monin & Yaglom 1975). This would mean that $\bar{\lambda}$ is proportional to the amplitude U of the flow for large U , which is clearly not the case here. In fact, Girimaji & Pope (1990) showed that, for a turbulent flow, the mean Lyapunov exponent is three times smaller than the mean positive stretching rate because of two effects. The first effect is due to the presence of the vorticity, which tends to rotate the diffuselet away from the direction of maximum stretching, as already apparent from the analysis in Corrsin & Karweit (1969). In our case, the vorticity is equal to the stretching rate since it is a pure shear. The stretching factor ρ can be calculated at late times (or at large U for a given time step $\Delta t = 1/2$) as $\sqrt{1 + \gamma^2 \Delta t^2} \approx |\gamma| \Delta t$. Averaging over a quarter of a wavelength gives $\langle \rho \rangle = 2U\Delta t$ from which the mean Lyapunov exponent can be deduced,

$$\bar{\lambda} = \frac{\log(2U\Delta t)}{\Delta t}. \quad (3.20)$$

This asymptotic prediction for a large velocity amplitude is plotted in figure 6 as a dashed line for $\Delta t = 1/2$. It is very close to the numerical and theoretical results despite the absence of averaging over the initial orientation. It proves that the logarithmic (rather than linear) dependence of the Lyapunov exponent with U at large velocity amplitudes clearly comes from the presence of the vorticity.

Girimaji & Pope (1990) found that there is a second effect contributing to the decreases of the Lyapunov exponent in turbulent flows: the finiteness of the persistent time. As a basic example, Duplat & Villermaux (2000) analysed the case of a stagnation point flow with amplitude γ . After a finite persistent time Δt the Lyapunov exponent averaged over all initial orientations is given by $\bar{\lambda}/\gamma = \ln(\cosh(\gamma\Delta t))/\gamma\Delta t$. For a large time step Δt , the Lyapunov exponent is exactly equal to the stretching rate γ . However, for a small time step, the ratio $\bar{\lambda}$ is proportional to $(\gamma\Delta t)\gamma \sim \gamma^2$. It indicates that at first order in $\gamma\Delta t$ a stagnation point flow does not stretch material lines in the mean because there are as many lines that are stretched than are compressed. After a finite time, the lines tend to align with the stretching direction such that there is more stretching than compression. In our case, we recover exactly the same scaling law $(U\Delta t)U$ for small amplitudes since $\bar{\lambda}$ scales as U^2 . In fact, this limit of small $U\Delta t$ corresponds to a flow delta correlated in time, also known as the Kraichnan flow. Kraichnan (1974) showed that the asymptotic value of the Lyapounov exponent is then

$$\lambda(t) = \frac{1}{d+2} \int_{-\infty}^t \langle \overline{\nabla u}_{ij}(t) \overline{\nabla u}_{ij}(t') \rangle dt', \quad (3.21)$$

where d is the dimension of space. For the sine flow, the velocity tensor is given by (3.5) for t between 0 and $1/2$ and t' varying between 0 and t . Averaging over the position x_i , the Lyapunov exponent is thus equal to $\pi^2 U^2 t/2$. The linear increase with time means that the flow must be applied during a finite time in order for the stretching to be efficient. Averaging for $0 < t < 1/2$ leads to a mean Lyapunov exponent

$$\bar{\lambda}_K = \frac{\pi^2 U^2}{8}. \quad (3.22)$$

This prediction is plotted as a black solid line in figure 6 and is in excellent agreement for small velocity amplitudes.

The variance is also plotted in figure 6 in red as a function of U . There is a very good agreement between the theory and the numerics at small velocity. At large U , the variance is slightly smaller than in the theory. It is striking to see that there is an exact relation between the Lyapunov exponent and the variance at small U ,

$$V(t) = \bar{\lambda}t. \quad (3.23)$$

This result is classical for the stretching factor of line elements in a Kraichnan flow. Indeed, Kraichnan (1974) states in his equation (2.33) that the ratio of the mean stretching factor $\bar{\lambda}t$ divided by half the variance $V/2$ is equal to the dimension of space (see also Balkovsky & Fouxon 1999; Meunier & Villermaux 2010). This property can be shown for a single diffuselet which experiences a small stretching (i.e. with μ_i close to 1). By noting that (2.31) can be rewritten as $P(\log \rho) = \exp(\log \rho)f(\log \rho)$ with f an even function, it can be shown that

$$\int_{-\log(\mu_i)/2}^{\log(\mu_i)/2} ue^u f(u) du = \int_{-\log(\mu_i)/2}^{\log(\mu_i)/2} u^2 e^u f(u) du \quad (3.24)$$

in the limit of small $\log \mu_i$ (replacing e^u by its Taylor expansion $1 + u$). As a consequence, the average and variance of $\log \rho$ are equal for small stretching rates. However, it is clear

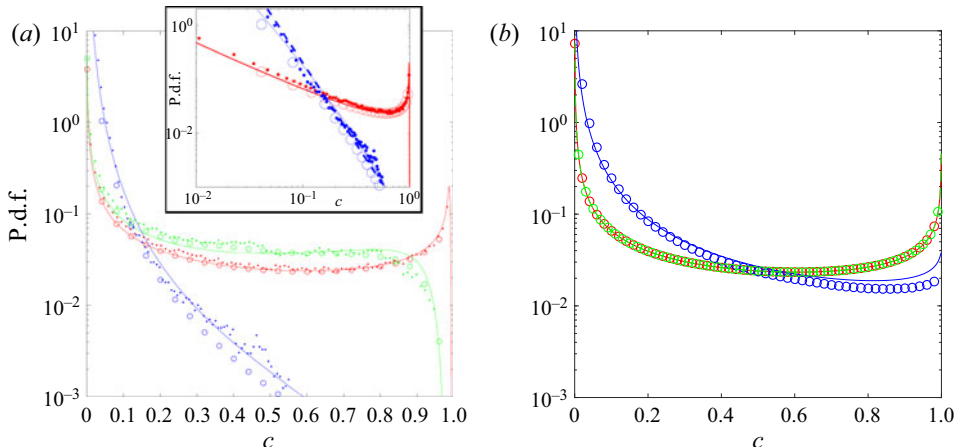


Figure 7. Probability distribution function of the scalar concentration for $U = 0.3$. The diffusivity is equal to $D = 10^{-6}$ for (a) and $D = 10^{-10}$ for (b). Times are equal to $t = 0.5$ (red), $t = 5$ (green) and $t = 50$ (blue). Solid lines correspond to the analytical formula (3.26) based on the log normal law (3.19) with the mean Lyapunov exponent and the variance given analytically by (3.17) and (3.18). Circles correspond to the numerical result using the diffuselet method given by (2.38). In (a) dots correspond to the numerical result averaged over five DNS simulations where the initial y position of the filament is varied between $\pi - 0.4$ and $\pi + 0.4$. The power law $1/c^3$ is plotted as a blue dashed line in the inset.

that this relation does not hold when U is larger than one. It corresponds to the case when the stretching is persistent on a longer time than the characteristic shear time $1/\gamma$, i.e. that the flow is no more delta correlated in time. In this regime, the variance saturates at a value close to 2 whereas the Lyapunov exponent increases logarithmically. The p.d.f. of stretching rates become thinner as U increases because all diffuselets are aligned with the shear (and, thus, within each other) at the end of each step.

3.3. Probability distribution function of concentration

The main advantage of the diffuselet technique is that it gives the concentration field in the presence of diffusion. We first focus on the p.d.f. of concentration that can be calculated without the reconstruction of the overall concentration field as long as the strip does not overlap with itself; this holds in the diluted limit, when aggregation phenomena can be neglected (see, e.g. § 6 in Meunier & Villermaux (2010) and Villermaux (2019)).

As mentioned at the end of § 3.1, the tensor \mathbf{T}_i can be obtained numerically using recurrence relations. Let $\eta_i > \eta'_i$ be its eigenvalues. The p.d.f. of concentration is given by (2.38) for each diffuselet and then averaged over all diffuselets. The resulting p.d.f. is plotted in figure 7 for different diffusivities for small velocity $U = 0.3$. The general features of the p.d.f. are classical. They are initially U-shaped corresponding to the Gaussian profile of the diffuselets. At later times, they become a decreasing function of the concentration in a time laps that depends on the diffusivity and on the stretching rate (i.e. the amplitude U). As time evolves, the p.d.f. becomes narrower since the maximal concentrations of the diffuselets decrease toward 0.

For the moderate diffusivity $D = 10^{-6}$ (see figure 7a), the numerical p.d.f. using diffuselets (plotted as open symbols) is compared with the result of the DNS (plotted as dots). For the comparison to be meaningful, we have chosen in the DNS a filament of thickness $s_0 = 0.01$ between $x = 0$ and $x = 1$ and in the diffuselet method 10^4 diffuselets

of thickness $s_0 = 0.01$ and of length $\delta\ell_0 = 10^{-4}$ (for the total length of all diffuselets to be equal to 1). There is an excellent agreement for the smallest velocity $U = 0.3$ except at late times for the largest concentrations. It should be noted that in the DNS, the final p.d.f. slightly fluctuates when the initial position of the filament is varied. This is why it is not clear that the DNS gives a universal result unless an ensemble average is done over all initial positions of the filament. Overall, the agreement between the two methods is very good over three decades.

As in Meunier & Villermaux (2010), it is possible to predict the concentration p.d.f. from the normal law of stretching factors (3.19). Indeed, if a diffuselet experiences a constant stretching rate, its striation thickness decreases exponentially in time such that its dimensionalised time τ_i only depends on the final stretching factor ρ ,

$$\tau_{th}(\rho) = 1 + \frac{2Dt}{s_0^2} \frac{\rho^2 - 1}{\log \rho}. \quad (3.25)$$

By doing so, we assume that the history of stretching (there are many ways to build a given ρ within a time t) has no effect. For a given stretching factor ρ , the diffuselet has thus a p.d.f. of concentration corresponding to the already used Gaussian profile $1/(c\sqrt{-\log(c\sqrt{\tau})})$ weighted by a factor $s_0\delta\ell_0\sqrt{\tau}$ corresponding to the surface of the diffuselet. The total p.d.f. of concentration is then obtained by convolution with the p.d.f. of stretching factors (3.19). It leads to a theoretical prediction of the p.d.f.,

$$P_{th}(c) = \frac{s_0 N \delta \ell_0}{c \sqrt{2\pi V_{th}(t)}} \int_{\tau_{th}(\rho) < c^{-2}} \exp\left[\frac{-(\log \rho - \bar{\lambda}t)^2}{2V_{th}(t)}\right] \frac{\sqrt{\tau_{th}(\rho)} d \log \rho}{\sqrt{-\log(c\sqrt{\tau_{th}(\rho)})}}. \quad (3.26)$$

The factor N comes from the sum over the N diffuselets; it ensures that $\int c P_{th}(c) dc$ is equal to the total quantity of the scalar. In Meunier & Villermaux (2010) the Lyapunov exponent $\bar{\lambda}$ was measured numerically from the stretching rate of the filament. Here, it is known theoretically from (3.17) and the variance is equal to $V_{th}(t) = 2tV_{1/2}$, with $V_{1/2}$ given by (3.18). This prediction is plotted in figure 7 as solid lines. It is in good agreement with the numerical results for $U = 0.3$ especially at early times where the difference between the diffuselet method and the theory is hardly visible. At late times, the maximum concentration $C = \tau_{th}(\rho)^{-1/2}$ scales as $1/\rho$ such that the p.d.f. of maximum concentration is equal to $Q(C) = P_{th}(\log \rho)/C^2$, with $\log \rho = -\log C$. Using the log normal form of the p.d.f. of stretching factor (3.19) leads to a power law for the p.d.f. of maximal concentration,

$$Q(c) \sim c^{-2 - \bar{\lambda}t/(2V)}. \quad (3.27)$$

In two dimensions the ratio $\bar{\lambda}t/(2V)$ is close to 1 such that the p.d.f. of concentration scales as c^{-3} . This is very well confirmed in the inset of figure 7.

Figure 8 shows the p.d.f. of concentration for a larger velocity $U = 3$. It is clear that the analytical model does not work at all. This is due to the discrepancy between the theoretical and numerical Lyapunov exponent, which has been explained in the previous subsection. However, the agreement between the DNS and diffuselet method is correct over two decades. At late times, the p.d.f. is again very close to the power law c^{-3} .

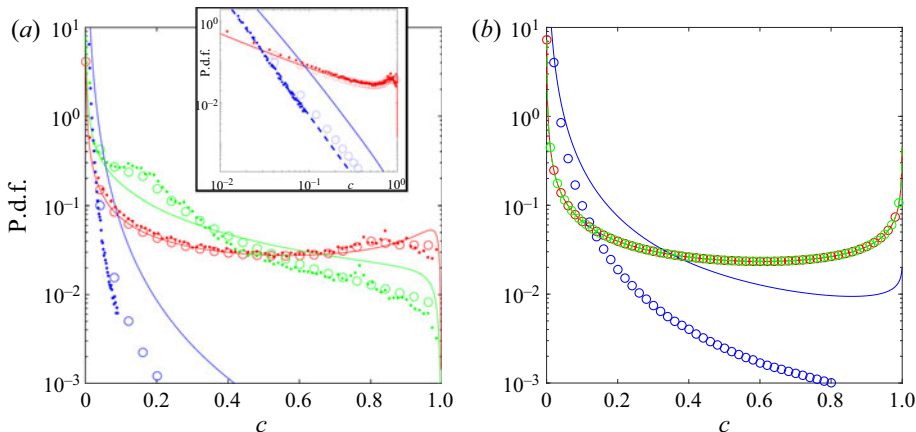


Figure 8. Probability distribution function of the scalar concentration for $U = 3$. The diffusivity is equal to $D = 10^{-6}$ for (a) and $D = 10^{-10}$ for (b). Times are equal to $t = 0.5$ (red), $t = 1$ (green) and $t = 4$ (blue). Solid lines correspond to the analytical formula (3.26) based on the log normal law (3.19) with the mean Lyapunov exponent and the variance given analytically by (3.17) and (3.18). Circles correspond to the numerical result using the diffuselet method given by (2.38). In (a) dots correspond to the numerical result averaged over four DNS where the initial filament is oriented at 0° , 45° , 90° and 135° with respect to the x axis. The power law $1/c^3$ is plotted as a blue dashed line in the inset.

Finally, it is possible to get theoretically the variance of concentration by integrating $\int c^2 P_{th}(c) dc$. It can be written as a simple integral

$$\langle c^2 \rangle = \frac{s_0 N \delta \ell_0}{2 \sqrt{V_{th}(t)}} \int_{-\infty}^{\infty} \exp\left[\frac{-(\log \rho - \bar{\lambda}t)^2}{2V_{th}(t)}\right] \frac{d \log \rho}{\sqrt{\tau_{th}(\rho)}}. \quad (3.28)$$

This prediction is plotted in figure 9 and compared with the numerical results. The overall features of the curves are classical. The variance of concentration remains constant until the mixing time that scales as $\log(U s_0 / D)$. It then decreases exponentially with a decay rate equal to $-(\bar{\lambda} - V/(2t))$. Indeed, it can be shown (by splitting the integral at $\rho = (\bar{\lambda}t)^{1/5}$) that the theoretical variance is asymptotically equal to

$$\langle c^2 \rangle \sim I \frac{s_0^2 N \delta \ell_0 V^{1/4}}{2^{3/4} \sqrt{Dt}} \exp\left(-\left(\bar{\lambda}t - \frac{V}{2}\right)\right) \quad (3.29)$$

at late times. The integral I is equal to $\int_0^{\infty} \sqrt{x} e^{-x^2} dx = 0.6127$ if $V = \bar{\lambda}t$ and equal to $\sqrt{\pi(\bar{\lambda}t - V)(2V)^{-1/4}}$ if $V < \bar{\lambda}t$.

For $U = 0.3$, there is a good agreement between the numerics and the theory despite a small overestimation of the theory. At large velocity $U = 3$, the theoretical prediction is very far from the numerics due to the wrong value of the Lyapunov exponent λ_{th} . It should be noted that the variance calculated by the DNS at $D = 10^{-6}$ is in good agreement with the diffuselet method at early times. At late times, it is either larger (for $U = 0.3$) or smaller (for $U = 3$) than the diffuselet method. It indicates that the DNS result is sensitive to the initial position of the filament such that an ensemble average over all positions would be necessary to get the ‘universal’ evolution of the variance for this sine flow.

This new numerical method gives the exact p.d.f. of Lyapunov exponents and of concentration in only a few seconds on a standard computer for any diffusivity. It has been compared with a new analytical prediction which works only for small velocity

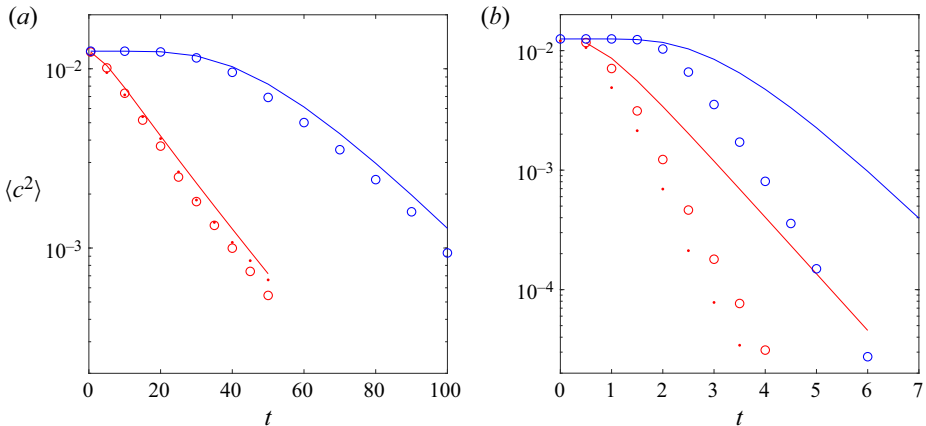


Figure 9. Variance of scalar concentration as a function of time for $U = 0.3$ (a) and $U = 3$ (b) and for $D = 10^{-6}$ (red) and $D = 10^{-10}$ (blue). Circles correspond to the numerical result using the diffuselet method whereas dots correspond to DNS simulations. Solid lines correspond to the analytical prediction (3.28) with λ given by (3.17) and $V_{th}(t) = 2tV_{1/2}$ given by (3.18).

amplitudes – corresponding to a Kraichnan flow, i.e. delta correlated in time – and for large velocity amplitudes – corresponding to a long persistent time.

4. Three-dimensional sine flow

4.1. Analytical formulae for the trajectories and the tensors of the diffuselets

In this section we apply the same technique developed above to the case of a 3-D random sine flow with a wavelength equal to 1. It is defined for the n th time interval by

$$\text{Step 1: } \mathbf{u} = U \begin{bmatrix} 0 \\ \sin[2\pi x + \chi_1(n)] \\ 0 \end{bmatrix} \quad \text{if } t \in \left[n; n + \frac{1}{3}\right], \quad (4.1)$$

$$\text{Step 2: } \mathbf{u} = U \begin{bmatrix} 0 \\ 0 \\ \sin[2\pi y + \chi_2(n)] \end{bmatrix} \quad \text{if } t \in \left[n + \frac{1}{3}; n + \frac{2}{3}\right], \quad (4.2)$$

$$\text{Step 3: } \mathbf{u} = U \begin{bmatrix} \sin[2\pi z + \chi_3(n)] \\ 0 \\ 0 \end{bmatrix} \quad \text{if } t \in \left[n + \frac{2}{3}; n + 1\right]. \quad (4.3)$$

The random phases χ_1 , χ_2 and χ_3 are fixed for all numerical simulations (see table 1 for the first ten values). The trajectory \mathbf{x}_i of a tracer initially at (x_0, y_0, z_0) can be easily integrated. Indeed, x_i is constant during step 1 (equal to $x_i(n)$) such that the y velocity is constant and $y_i(t) = y_i(n) + U(t - n) \sin[2\pi x_i(n) + \chi_1(n)]$. Similarly, y_i is constant during step 2 such that the z velocity is constant and $z_i(t) = z_i(n) + U(t - n - 1/3) \sin[2\pi y_i(n + 1/3) + \chi_2(n)]$, where we have used the fact that $x_i(n + 1/3) = x_i(n)$. It should be noted that y_i is constant during steps 2 and 3 such that $y_i(n + 1/3) = y_i(n + 1)$. Finally, z_i is constant during step 3 such that its x velocity is constant and $x_i(t) = x_i(n) + U(t - n - 2/3) \sin[2\pi z_i(n + 2/3) + \chi_3(n)]$, where we have used the fact that $x_i(n + 2/3) = x_i(n)$.

n	1	2	3	4	5	6	7	7	8	9
χ_1	3.6721	5.6535	4.7744	1.8854	5.8522	2.5802	4.2842	4.7991	4.0560	3.9965
χ_2	0.9283	5.9748	0.2954	5.0034	1.5375	4.3288	1.1735	4.2946	5.4568	0.7893
χ_3	5.1191	5.6913	0.7979	5.7389	3.9732	0.6129	1.7499	3.4362	6.0162	6.0626

Table 1. Phases for the 2-D and 3-D sine flow.

To conclude, the positions at time $t = n$ are simply obtained numerically by applying the formulae

$$y_i(n+1) = y_i(n) + \frac{U}{3} \sin[2\pi x_i(n) + \chi_1(n)], \quad (4.4)$$

$$z_i(n+1) = z_i(n) + \frac{U}{3} \sin[2\pi y_i(n+1) + \chi_2(n)], \quad (4.5)$$

$$x_i(n+1) = x_i(n) + \frac{U}{3} \sin[2\pi z_i(n+1) + \chi_3(n)], \quad (4.6)$$

for $n = 0, 1, 2, \dots, T_{max}$.

We now calculate the tensors \mathbf{L}_i and \mathbf{T}_i analytically. We first focus on the first step. During step 1, x_i is constant such that the velocity gradient is constant and equal to

$$\overline{\nabla u} = \begin{bmatrix} 0 & 0 & 0 \\ \gamma & 0 & 0 \\ 0 & 0 & 0 \end{bmatrix}, \quad \text{with } \gamma = 2\pi U \cos[2\pi x_i(n) + \chi_1(n)]. \quad (4.7)$$

The tensor $\mathbf{L}_i(t)$ is given by an exponential matrix $\exp[-\int \overline{\nabla u}^* dt] \mathbf{L}_i(n)$ that is simply equal to $[\mathbf{I} - (t-n)\overline{\nabla u}^*] \mathbf{L}_i(n)$ since $\overline{\nabla u}^{*2}$ vanishes. During step 1, the tensor reads

$$\mathbf{L}_i(t) = \begin{bmatrix} 1 & -\gamma(t-n) & 0 \\ 0 & 1 & 0 \\ 0 & 0 & 1 \end{bmatrix} \mathbf{L}_i(n), \quad \text{with } \gamma = 2\pi U \cos[2\pi x_i(n) + \chi_1(n)]. \quad (4.8)$$

It is then easy to compute the tensor \mathbf{T}_i from (2.23). At time $t = n + 1/3$ it reads

$$\mathbf{T}_i\left(n + \frac{1}{3}\right) = \mathbf{T}_i(n) + \frac{4D}{s_0^2} \mathbf{L}_i^*(n) \begin{bmatrix} \frac{1}{3} & -\frac{\gamma}{18} & 0 \\ -\frac{\gamma}{18} & \frac{1}{3} + \frac{\gamma^2}{81} & 0 \\ 0 & 0 & \frac{1}{3} \end{bmatrix} \mathbf{L}_i(n). \quad (4.9)$$

For the second step, the technique is similar although the formulae are slightly different. We find that

$$\mathbf{L}_i(t) = \begin{bmatrix} 1 & 0 & 0 \\ 0 & 1 & -\gamma\left(t-n-\frac{1}{3}\right) \\ 0 & 0 & 1 \end{bmatrix} \mathbf{L}_i\left(n + \frac{1}{3}\right), \quad (4.10)$$

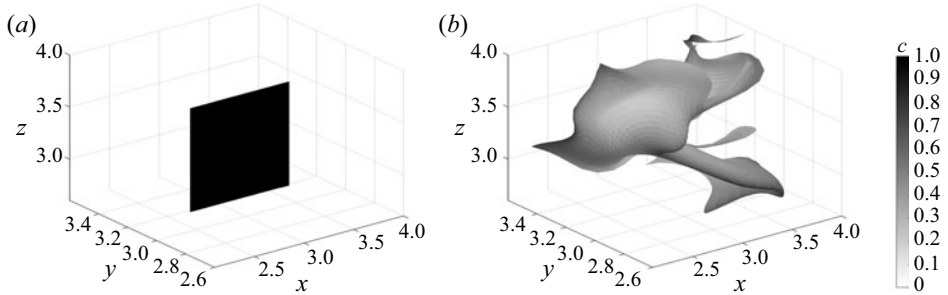


Figure 10. Three-dimensional plot of a scalar sheet initially located along the (x, z) plane (a) and advected until $t = 15$ (b) by a 3-D sine flow with $U = 0.3$ and $D = 10^{-6}$. The initial thickness of the sheet is $s_0 = 0.01$.

with $\gamma = 2\pi U \cos[2\pi y_i(n+1) + \chi_2(n)]$ and

$$\boldsymbol{\tau}_i\left(n + \frac{2}{3}\right) = \boldsymbol{\tau}_i\left(n + \frac{1}{3}\right) + \frac{4D}{s_0^2} \boldsymbol{L}_i^* \left(n + \frac{1}{3}\right) \begin{bmatrix} \frac{1}{3} & 0 & 0 \\ 0 & \frac{1}{3} & -\frac{\gamma}{18} \\ 0 & -\frac{\gamma}{18} & \frac{1}{3} + \frac{\gamma^2}{81} \end{bmatrix} \boldsymbol{L}_i \left(n + \frac{1}{3}\right). \quad (4.11)$$

For the third step, we find that

$$\boldsymbol{L}_i(t) = \begin{bmatrix} 1 & 0 & 0 \\ 0 & 1 & 0 \\ -\gamma \left(t - n - \frac{2}{3}\right) & 0 & 1 \end{bmatrix} \boldsymbol{L}_i \left(n + \frac{2}{3}\right), \quad (4.12)$$

with $\gamma = 2\pi U \cos[2\pi y_i(n+1) + \chi_2(n)]$ and

$$\boldsymbol{\tau}_i(n+1) = \boldsymbol{\tau}_i\left(n + \frac{2}{3}\right) + \frac{4D}{s_0^2} \boldsymbol{L}_i^* \left(n + \frac{2}{3}\right) \begin{bmatrix} \frac{1}{3} + \frac{\gamma^2}{81} & 0 & -\frac{\gamma}{18} \\ 0 & \frac{1}{3} & 0 \\ -\frac{\gamma}{18} & 0 & \frac{1}{3} \end{bmatrix} \boldsymbol{L}_i \left(n + \frac{2}{3}\right). \quad (4.13)$$

To conclude, the tensors can be calculated from time n to time $n+1$ by applying successively (4.8) at time $t = n + 1/3$, (4.9), (4.10) at time $t = n + 2/3$, (4.11), (4.12) at time $t = n + 1$ and (4.13). The initial values are simply $\boldsymbol{L}(0) = \boldsymbol{\tau}(0) = \boldsymbol{I}$. This procedure is extremely fast because there is no temporal integration in each time interval. It is thus possible to obtain the trajectories of 8000 diffuselets over 15 periods in only 5 s. If the diffuselets are initially located in an (x, z) plane, it permits us to reconstruct the evolution of a diffusive sheet. An example is plotted in figure 10 for a moderate diffusivity $D = 10^{-6}$. The sheet is folded and stretched, enhancing its diffusion. The concentration along the sheet has decreased by a factor two after only 15 periods.

The concentration field is compared with the result of DNS computed for a 1024^3 mesh and with a time interval of 1/30th of a period. The CPU time for this simulation is equal to approximately 70 h that is 50 000 times slower than the diffuselet method. The comparison

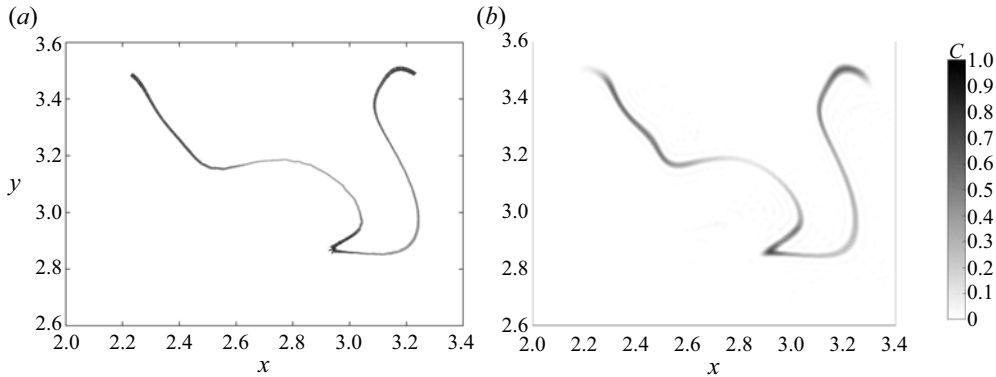


Figure 11. Two-dimensional concentration field in the (x, y) plane at $z = \pi$ obtained (a) by the diffuselet method and (b) by DNS. The scalar initially at $y = \pi$ with $(x, z) \in [\pi - 0.5, \pi + 0.5]^2$ is advected until $t = 15$ by the 3-D sine flow with $U = 0.3$, $D = 10^{-6}$ and $s_0 = 0.01$ as in figure 10.

between the two methods is plotted in figure 11. The position of the sheet is well captured by the diffuselet method. However, the concentration seems to be slightly smaller in the DNS than in the diffuselet method. It probably comes from numerical diffusion in the DNS due to the under-resolved mesh. Indeed, applying the convergence criterion obtained in two dimensions (see figure 18a), the error for this DNS can be assumed to be of the order 50 % despite the large memory used (equal to 16GB for $N = 1024$).

4.2. Probability distribution function of stretching

As shown previously, the stretching factor $\rho = \delta A_i / \delta A_0$ for each diffuselet is simply given by the square root of $\mathbf{n}_0^* \mathbf{L}_i^* \mathbf{L}_i \mathbf{n}_0$. When averaging over all initial orientations \mathbf{n}_0 and all diffuselets, the p.d.f. of stretching factors is given in three dimensions by ((2.46) and (2.47)), where $\mu_i > \mu'_i > \mu''_i$ are the three eigenvalues of $\mathbf{L}_i^* \mathbf{L}_i$. This p.d.f. is plotted as dotted symbols in figure 12 at different times for a small velocity $U = 0.3$ (top plots) and a large velocity $U = 3$ (bottom plots). After a third of a period, the p.d.f. has a cusp around 0. This singularity is due to the diffuselets which have not been stretched (whatever their initial orientation) since they are at a position where the shear $\gamma = \partial v / \partial x$ vanishes. After one period, the probability that a diffuselet has experienced no shear is small such that this singularity has disappeared (green symbols). As time evolves the p.d.f.s become more and more round. At late times the p.d.f.s are parabolic with a maximum located at a position increasing linearly in time. This is exactly similar to the 2-D case with a mean Lyapunov exponent $\bar{\lambda} = \langle \log \rho \rangle / t$ constant in time as classically obtained for chaotic flows. The variance of these distributions $V = \langle (\log \rho - \bar{\lambda}t)^2 \rangle$ also increases linearly in time as obtained by $3n$ independent stretching processes.

It is possible to calculate analytically the p.d.f. of stretching factors at the end of the first step. Indeed, (4.8) gives at time $t = 1/3$,

$$\mathbf{L}_i^* \mathbf{L}_i = \begin{bmatrix} 1 & -\frac{\gamma}{3} & 0 \\ -\frac{\gamma}{3} & 1 + \frac{\gamma^2}{9} & 0 \\ 0 & 0 & 1 \end{bmatrix}, \quad \text{with } \gamma = 2\pi U \cos[2\pi x_0 + \chi_1(1)], \quad (4.14)$$

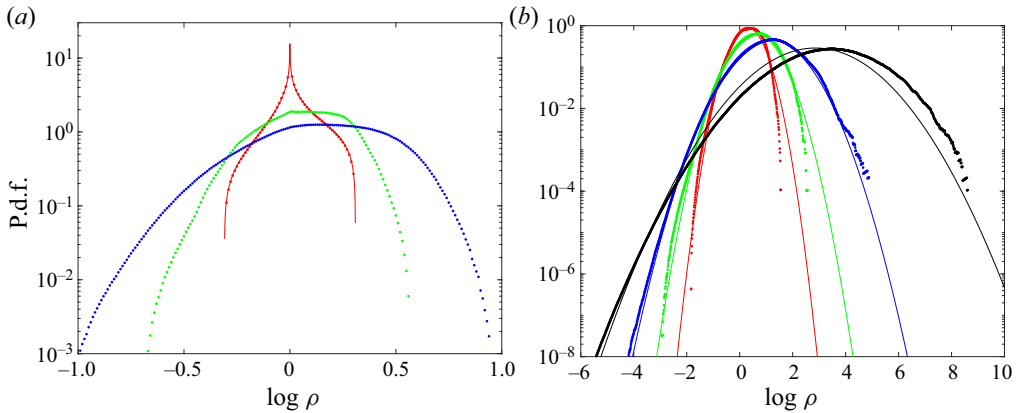


Figure 12. Probability distribution function of the stretching rate for $U = 0.3$ at times $t = 0.5$ (red), $t = 1$ (green) and $t = 2$ (blue) in (a); and at times $t = 5$ (red), $t = 10$ (green), $t = 20$ (blue) and $t = 50$ (black) in (b). Solid lines correspond to the exact calculation ((4.17) and (4.18)) at $t = 1/3$ and to the normal law (4.21) at late times with the mean Lyapunov exponent and the variance given analytically by (4.19) and (4.20).

which has eigenvalues equal to $\mu = 1 + \gamma^2(1 + \sqrt{1 + 36/\gamma^2})/18$ larger than 1, $\mu' = 1$ and $\mu'' = 1/\mu$. This expression can be inverted to find the initial position x_0 corresponding to an eigenvalue μ ,

$$x_0 = \frac{1}{2\pi} \arccos \left(\frac{3(\mu - 1)}{2\pi U \sqrt{\mu}} \right) - \frac{\chi_1(1)}{2\pi}. \quad (4.15)$$

The probability to have an eigenvalue μ is given by $P(\mu) d\mu = dx_0/(1/4)$ with x_0 uniformly distributed over a fourth of a wavelength (between $-(\chi_1(1)/2\pi)$ and $-(\chi_1(1)/2\pi) + 1/4$). Differentiating (4.15) with respect to μ leads to the p.d.f. of eigenvalue

$$P(\mu) = \frac{\mu + 1}{\pi \mu \sqrt{4\pi^2 U^2 \mu/9 - (\mu - 1)^2}}. \quad (4.16)$$

Convoluting this formula with the probability to have a stretching factor ((2.46) and (2.47)) and multiplying by ρ (to get the p.d.f. of $\log \rho$) leads to an analytic formula at $t = 1/3$,

$$P_{1/3}(\log \rho) = \int_{\mu=\rho^2}^{\mu_M} \frac{(\mu + 1)\rho^2 F[2(\rho^2 - 1)(\mu + 1)/(\mu - \rho^2)]}{\pi^2 \mu \sqrt{4\pi^2 U^2 \mu/9 - (\mu - 1)^2} \sqrt{\mu - \rho^2} \sqrt{1 - \mu^{-1}}} \quad \text{for } \rho > 1, \quad (4.17)$$

$$P_{1/3}(\log \rho) = \int_{\mu=\rho^{-2}}^{\mu_M} \frac{(\mu + 1)\rho^2 F[2(1 - \rho^2)(\mu + 1)/(\rho^2 \mu - 1)]}{\pi^2 \mu \sqrt{4\pi^2 U^2 \mu/9 - (\mu - 1)^2} \sqrt{\mu - 1} \sqrt{\rho^2 - \mu^{-1}}} \quad \text{for } \rho < 1, \quad (4.18)$$

with $\mu_M = 1 + 4\pi^2 U^2 (1 + \sqrt{1 + 36/(4\pi^2 U^2)})/18$. This analytical prediction at time $t = 1/3$ is plotted in figure 12(a) as a red line for $U = 0.3$. There is an excellent agreement with the numerical p.d.f. plotted as red dots.

From this analytical p.d.f. it is possible to calculate the mean Lyapunov exponent as the first moment of the p.d.f. However, it is easier to use (2.41) and to replace the discrete sum over the diffuselets by an integral $\int P(\mu) d\mu$. Since the eigenvalues at $t = 1/3$ are equal

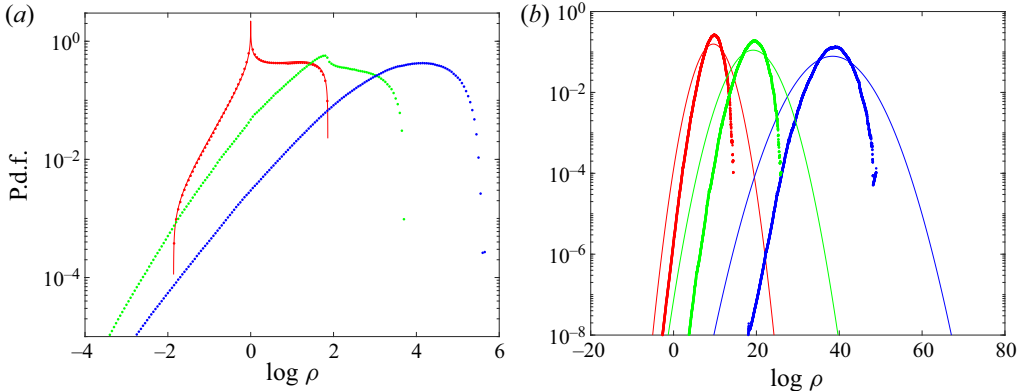


Figure 13. Probability distribution function of the stretching rate for $U = 3$ at times $t = 0.5$ (red), $t = 1$ (green) and $t = 2$ (blue) in (a); and at times $t = 5$ (red), $t = 10$ (green), $t = 20$ (blue) and $t = 50$ (black) in (b). Solid lines correspond to the exact calculation ((4.17) and (4.18)) at $t = 1/3$ and to the normal law (4.21) at late times with the mean Lyapunov exponent and the variance given analytically by (4.19) and (4.20).

to μ , 1 and $1/\mu$, it takes the simple form

$$\bar{\lambda}_{th} = \int_{\mu=1}^{\mu_M} \int_{\phi=0}^{\pi/2} \int_{\theta=0}^{\pi/2} P(\mu) \frac{\log [\mu + (1-\mu)(\mu + \sin^2 \phi) \sin^2 \theta / \mu]}{2/3} \frac{\sin \theta d\theta d\phi d\mu}{\pi/2}. \quad (4.19)$$

The variance of the distribution can also be calculated numerically as

$$V_{1/3} = \int_{\mu=1}^{\mu_M} \int_{\phi=0}^{\pi/2} \int_{\theta=0}^{\pi/2} P(\mu) \frac{\log [\mu + (1-\mu)(\mu + \sin^2 \phi) \sin^2 \theta / \mu]^2}{4} \frac{\sin \theta d\theta d\phi d\mu}{\pi/2} - \frac{\bar{\lambda}_{th}^2}{9} \quad (4.20)$$

at time $t = 1/3$. These theoretical results can then be used to infer the p.d.f. of stretching rates at late times. After n periods, if the $3n$ stretching steps are independent random processes, the p.d.f. of $\log \rho$ must be a normal law,

$$P_{th}(\log \rho) = \frac{1}{\sqrt{2\pi V_{th}(t)}} \exp \left[-\frac{(\log \rho - \bar{\lambda}_{th}t)^2}{2V_{th}(t)} \right], \quad \text{with } V_{th}(t) = 3tV_{1/3}, \quad (4.21)$$

which is the same formula as in two dimensions. This prediction is plotted as a solid line in figure 12(b). There is an excellent agreement with the numerical results for $U = 0.3$. The position and width of the parabola are similar between the numerics and theory. However, when the amplitude of the velocity is increased to $U = 3$, figure 13 shows that there is a clear discrepancy by a factor two at late times although the prediction is correct for $t = 1/3$. It indicates that the stretching steps are not independent random processes.

In order to analyse this discrepancy, the mean Lyapunov exponent is plotted in blue as a function of U in figure 14. The numerical values (plotted as symbols) are in good agreement with the theory (plotted as a black line) despite the saturation found for U larger than 1.

Kraichnan's prediction (3.21) for small velocity U can be applied for t between 0 and $1/3$ and t' varying between 0 and t . Averaging over the position x_i , the Lyapunov exponent

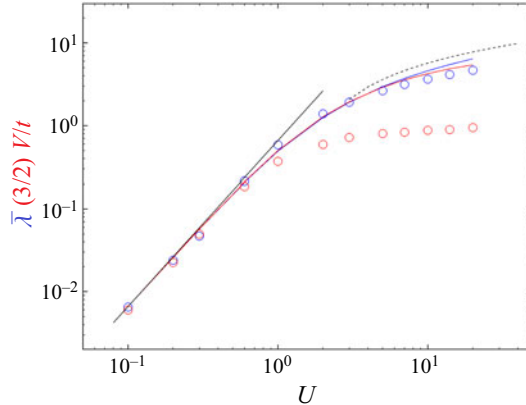


Figure 14. Mean Lyapunov exponent $\bar{\lambda} = \langle \log \rho \rangle / t$ (blue) and variance $V = \langle (\log \rho - \bar{\lambda}t)^2 \rangle$ (red) as a function of the velocity of the sine flow U . Solid lines correspond to the theoretical predictions calculated at $t = 0.5$ using (4.19) and (4.20). Numerical results averaged between $t = 20$ and $t = 50$ are plotted as symbols. The black line corresponds to Kraichnan's prediction (4.22).

is thus equal to $2\pi^2 U^2 t/5$. Averaging for $0 < t < 1/3$ leads to a mean Lyapunov exponent

$$\bar{\lambda}_K = \frac{\pi^2 U^2}{15}, \quad (4.22)$$

which is plotted as a black solid line in figure 6. There is an excellent agreement for small velocity amplitudes.

For a large velocity amplitude, the stretching rate decays at the end of each step due to the alignment of the diffuselets with the shear. The mean Lyapunov exponent increases logarithmically with U as in two dimensions. The prediction (3.20) is plotted in figure 14 for $\Delta t = 1/3$. There is a fair agreement, proving the logarithmic dependence on U .

The variance is also plotted in figure 14 in red as a function of U . There is a very good agreement between the theory and numerics at small velocity. At large U , the variance is smaller than in the theory. As in two dimensions, there is an exact relation between the Lyapunov exponent and the variance at small U ,

$$\bar{\lambda}t = \frac{3}{2}V(t). \quad (4.23)$$

This result is similar to the result by Kraichnan (1974) stating in his equation (2.33) that the ratio $\bar{\lambda}t$ divided by half the variance $V/2$ is equal to the dimension of space (see also Balkovsky & Fouxon 1999; Meunier & Villermaux 2010). However, this relation is obtained here for the stretching factor of surface elements rather than the stretching factor of line elements as in Kraichnan (1974).

Figure 14 indicates that this relation does not hold when U is larger than one: the numerical variance tends to saturate at a value close to 1 while the theoretical variance calculated at $t = 1/3$ increases logarithmically. It corresponds to the case when the stretching is persistent on a longer time than the characteristic stretching time, i.e. that the flow is no more delta correlated in time. In this regime all the diffuselets are aligned with each other at the end of each step such that the variance of the p.d.f. strongly decreases. This effect is probably cumulative which could explain the difference between the theory and numerics.

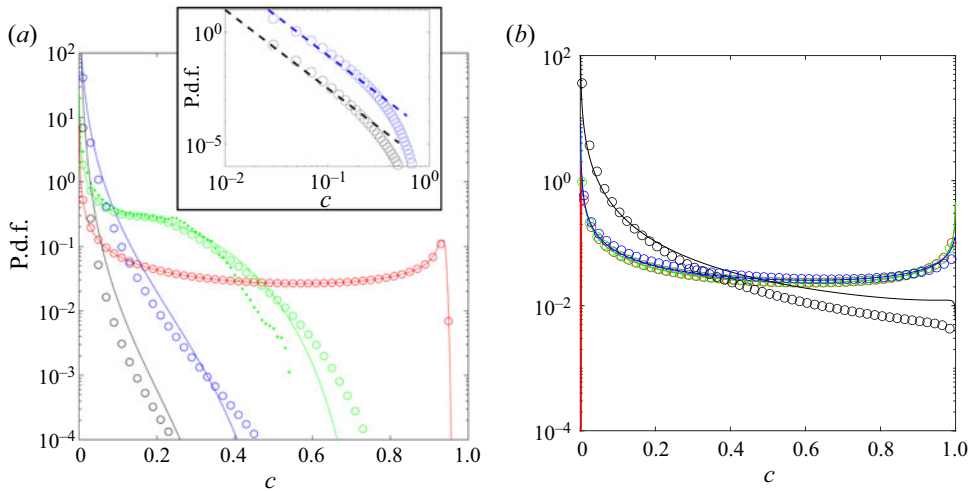


Figure 15. Probability distribution function of the scalar concentration for $U = 0.3$. The diffusivity is equal to (a) $D = 10^{-5}$ and (b) $D = 10^{-10}$. Times are equal to $t = 1/3$ (red), $t = 5$ (green), $t = 50$ (blue) and $t = 100$ (back). Solid lines correspond to the analytical formula (3.26) based on the log normal law (3.19) with the mean Lyapunov exponent and the variance given analytically by (4.19) and (4.20). Circles correspond to the numerical result using the diffuselet method given by (2.60). In (a) dots correspond to the numerical result obtained by DNS and the power law $1/c^{3.5}$ is plotted as a blue dashed line in the inset.

This result is in fact very similar to the 2-D case. For small U , the Lyapunov exponent $\bar{\lambda}$ and the variance divided by t both increase quadratically with U , and their ratio equals $d/2$ (where d is the dimension of space). For large U , the Lyapunov exponent increases logarithmically whereas the variance divided by t seems to saturate at a value close to unity. The only difference is that the theory works fairly in two dimensions (within 50 %) but strongly fails in three dimensions.

4.3. Probability distribution function of concentration

As in two dimensions, the p.d.f. of concentration can be calculated from the eigenvalues $\eta_i > \eta'_i > \eta''_i$ of the tensor \mathbf{T}_i , which is obtained from the recurrence relations of subsection 4.1. The p.d.f. of concentration is given by (2.60) for each diffuselet and then averaged over all diffuselets. The resulting p.d.f. is plotted in figure 15 for different diffusivities for small velocity $U = 0.3$ as symbols. At early times, the p.d.f.s are U-shaped corresponding to the Gaussian profile of the diffuselets. At later times they become a decreasing function of the concentration in a time laps that depends on the diffusivity. As time evolves, the p.d.f. becomes narrower since the maximal concentrations of the diffuselets decrease toward 0.

For the moderate diffusivity $D = 10^{-6}$ (see figure 15a), the numerical p.d.f. using diffuselets (plotted as open symbols) is compared with the result of the DNS (plotted as dots). For the comparison to be meaningful, we have chosen in the DNS an initial Gaussian sheet of thickness $s_0 = 0.01$ located at $y = \pi$ for x and z varying between $\pi - 0.5$ and $\pi + 0.5$, and in the diffuselet method 10^4 diffuselets of thickness $s_0 = 0.01$ and of area $\delta A_0 = 10^{-4}$ are taken (for the total area of all diffuselets to be equal to 1 as in the DNS). There is a fair agreement despite fluctuations of the DNS values around the diffuselet values. This could be due to the particular case considered in the DNS by contrast to

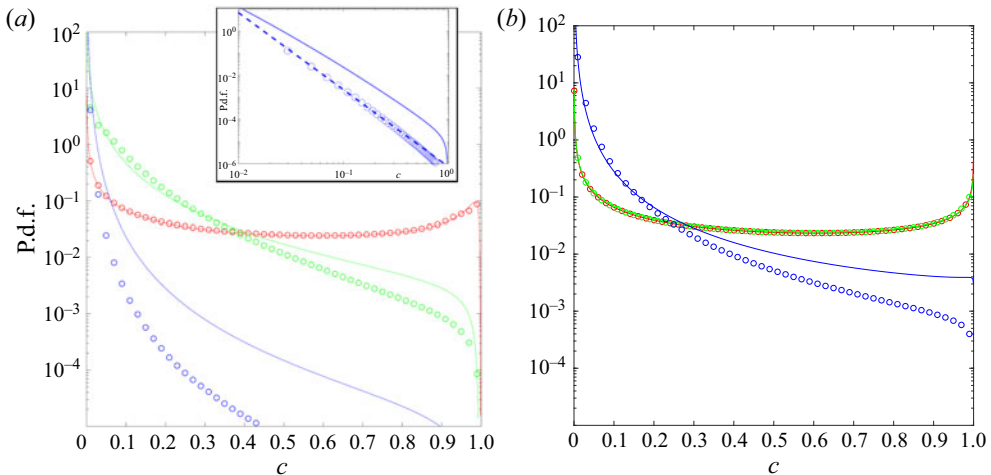


Figure 16. Probability distribution function of the scalar concentration for $U = 3$. The diffusivity is equal to $D = 10^{-6}$ (a) and $D = 10^{-10}$ (b). Times are equal to $t = 1/3$ (red), $t = 2$ (green) and $t = 5$ (blue). Solid lines correspond to the analytical formula (3.26) based on the log normal law (3.19) with the mean Lyapunov exponent and the variance given analytically by (3.17) and (3.18). Circles correspond to the numerical result using the diffuselet method given by (2.60). In (a) the power law $1/c^{3.5}$ is plotted as a blue dashed line in the inset.

the ensemble-averaged (over initial injection) case considered in the diffuselet method. The case of a larger velocity $U = 3$ is plotted in figure 16 for two different diffusivities. The same trend is observed although they are obtained much faster than for $U = 0.3$.

As in two dimensions, it is possible to give an analytic prediction of the p.d.f. of concentration since the p.d.f. of stretching factors is log normal. The same formula (3.26) is thus valid in three dimensions with $\delta\ell_0$ replaced by δA_0 . Here, the Lyapunov exponent $\bar{\lambda}$ is known theoretically from (4.19) and the variance is equal to $V_{th}(t) = 3tV_{1/3}$ with $V_{1/3}$ given by (4.20). This prediction is plotted in figures 15 and 16 as solid lines. It is in excellent agreement with the diffuselet method for $U = 0.3$ at early times. However, the agreement is only qualitative at late times. The p.d.f. is algebraic at late times with an exponent $-2 - \bar{\lambda}t/(2V)$ that is equal to $-2 - 3/2 = -3.5$ in three dimensions, whereas it was equal to -3 in two dimensions. As shown in the inset, this prediction is in excellent agreement with the results of the diffuselet method.

Finally, the variance of concentration is plotted in figure 17. It is given by (3.28) theoretically and compared with the diffuselet results. As in two dimensions, the variance remains constant until it reaches the mixing time which scales as $\log(Us_0/D)$. It then decreases exponentially with a decay rate equal to $\bar{\lambda} - V/(2t)$. For small velocity $U = 0.3$, the Lyapunov exponent and the variance are well predicted by Kraichnan through (4.22) and (4.23), which leads to a very simple expression for the decay rate $2\pi^2 U^2/45$. This prediction, plotted as a dashed line, is very close to our theoretical prediction, plotted as a dash-dotted line for $U = 0.3$. However, the two predictions are very different for a larger velocity $U = 3$. Kraichnan's prediction indeed failed because the Lyapunov exponent saturates at large U , as explained in the previous subsection. However, the theoretical prediction (dash-dotted line) also fails since it underestimates the decay rate. This can be explained since the variance obtained numerically by the diffuselet method is much smaller than predicted theoretically at $t = 1/3$. It thus seems that the correct decay rate should be equal to $\bar{\lambda}$ at large U (since V/t is negligible). This final prediction is plotted

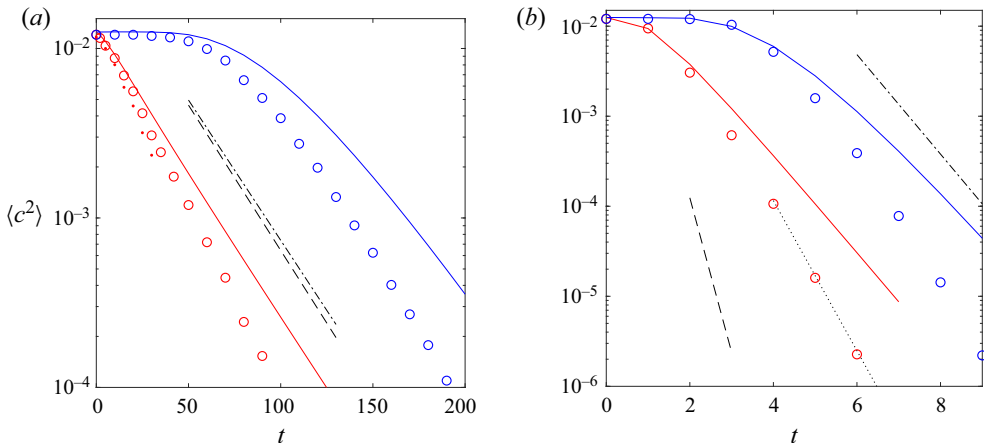


Figure 17. Variance of the scalar concentration as a function of time for $U = 0.3$ (a) and $U = 3$ (b) and for $D = 10^{-6}$ (red) and $D = 10^{-10}$ (blue). Circles correspond to the numerical result using diffuselet whereas dots correspond to DNS simulations. Solid lines correspond to the analytical prediction (3.28) with $\bar{\lambda}$ given by (4.19) and $V_{th}(t) = 3tV_{1/3}$ given by (4.20). The dash-dotted line corresponds to a decay rate $\bar{\lambda}_{th} - V_{th}/t$ and the dotted line to a decay rate $\bar{\lambda}_{th}$. The dashed line corresponds to a decay rate $2\bar{\lambda}_K/3$ with $\bar{\lambda}_K$ given by (4.22) valid for a Kraichnan flow.

as a dotted line in figure 17. It should be noted that the variance calculated by the DNS at $D = 10^{-6}$ is in good agreement with the diffuselet method at early times.

5. Conclusion

The advection–diffusion of a small surface element, called diffuselet, has been solved explicitly using the Ranz transform. As a first step, the stretching of material surfaces is calculated from the integrated velocity gradient tensor \mathbf{L}_i in (2.20), in a way similar to the calculation of material line stretching. The Lyapunov exponent of material surfaces can be averaged over all diffuselets and all initial orientations of the surface, leading to a simple formula (2.41) depending on the three eigenvalues μ_i , μ'_i and μ''_i of the tensor $\mathbf{L}_i^* \mathbf{L}_i$. Since the stretching of these surfaces corresponds to the compression rate in the normal direction, the Ranz transform can be applied in a second step. The maximal concentration and the spatial extent of the diffuselet is obtained analytically as a function of a time tensor \mathbf{T}_i easily derived from \mathbf{L}_i using (2.23). This solution is equal to the Green function given by Balkovsky & Fouxon (1999) for a point source, but is easier to compute numerically. These diffuselets can be averaged over all initial orientations to get the variance (2.53) and the p.d.f. of concentration (2.60) from the three eigenvalues η_i , η'_i and η''_i of the time tensor \mathbf{T}_i .

This method is then applied to a 2-D and a 3-D sine flow, where the positions and the tensors of the diffuselets can be derived analytically from one step to the other with no temporal integration. The statistics of Lyapunov exponents and of concentration can thus be calculated within a few seconds, i.e. orders of magnitude faster than with a DNS. The p.d.f. of stretching factor ρ is log normal, in agreement with discrete random stretching steps. The mean and variance of the p.d.f. of $\log \rho$ increase linearly in time, as suggested by the central limit theorem. The Lyapunov exponent can thus be predicted analytically from the exact calculation at the first step, given by (3.17) in two dimensions and (4.19) in three dimensions. These predictions are in good agreement with the numerical values (given

by the diffuselet method) for small and large velocity amplitudes. However, this theory underestimates the Lyapunov exponent by approximately 30 % for a moderate velocity amplitude because the diffuselets are not randomly oriented at the beginning of each step, as assumed in the theory. The variance of $\log \rho$ is also predicted analytically from the exact calculation at the first step, as given by (3.18) in two dimensions and (4.20) in three dimensions. There is an excellent agreement with the numerical values for a small velocity amplitude. This regime corresponds to the case of delta-correlated flows described by Kraichnan (1974) for which the variance is equal to $2\bar{\lambda}t/d$, with d the dimension of space. This prediction is in excellent agreement with our theoretical and numerical results for small velocity (displacement) amplitude. However, our numerical results indicate that the variance of $\log \rho$ is much smaller for a large velocity (displacement) amplitude. This is because all the diffuselets tend to be aligned at the end of each step and so have the same evolution, thus reducing the variance. From these statistics of stretching, the variance and the p.d.f. of concentration can be obtained theoretically and numerically. They have been compared successfully to the DNS results for moderate diffusivities. After a mixing time scaling as the logarithm of the Péclet number, the variance decays exponentially with a decay rate equal to $\bar{\lambda} - V/(2t)$, as shown in (3.29).

For a pure stagnation point flow, the Lyapunov exponent λ is exactly equal to the stretching rate γ . Here, it is interesting to note that λ is smaller than γ because the material lines/surfaces are not aligned with the stretching direction. As already noted by Girimaji & Pope (1990) for a turbulent flow, this comes from (i) the presence of vorticity and (ii) the fact that the time step Δt is finite. When the deformation of each step is small, the ratio λ/γ is proportional to $\gamma \Delta t$, as predicted by Kraichnan (1974). This ratio then saturates for large $\gamma \Delta t$. In a turbulent flow $\gamma \Delta t$ is intermediate, leading to a ratio $\lambda/\gamma \approx 0.3$ (Girimaji & Pope 1990) with a mean stretching rate $\gamma \approx 0.4/\tau_K$, where τ_K is the Kolmogorov time. Using this empirical measurement of the Lyapunov exponent in the Batchelor regime, it is possible to give an analytical formula (3.28) for the variance of concentration and an analytical formula (3.26) for the p.d.f. of concentration. In these formulae the Lyapunov exponent $\bar{\lambda}$ is empirically taken equal to $0.17/\tau_K$ and the variance V_{th} of stretching rate equal to $0.11t/\tau_K$, as given by Girimaji & Pope (1990). It should be noted that the ratio $\bar{\lambda}t/V_{th}$ is very close to $d/2$ (with d the dimension of space), as predicted by Kraichnan (1974) for a white noise-like flow.

To close, we need to make two remarks regarding the domain of strict applicability of this method, and of its interest beyond. First, the above blunt predictions for the variance and the p.d.f. are only valid for isolated diffuselets, i.e. for small initial blobs of scalar remaining isolated in the course of their advection by the flow. This excludes, if one wants to use these raw results, interaction between different diffuselets originating from different parts of the flow, and self-interacting diffuselets (see our second point below). Upon interaction, namely when two diffuselets, or parts of them, have been brought by the flow sufficiently close to each other so that their diffusive boundaries overlap, we know that the ingredients ruling the concentration field are no more diffusion and stretching, but that the aggregation of the diffuselets directs the route of the mixture towards uniformity. In that case, formulae (3.28) for the variance of scalar concentration and (3.26) for the p.d.f. of scalar concentration are not valid anymore, and are replaced by others accounting for the convolution of the interacting fields (Duplat, Jouary & Villermieux 2010b). However, in this aggregated or ‘well-mixed’ regime the total scalar field can still be reconstructed using the diffuselet concept, and it needs to be. In this respect, the concept of diffusion line element developed by Wang & Peters (2006) may be useful to describe the spatially smooth (with no voids) scalar field, made of an aggregation of diffuselets.

Second, the diffuselet concept described here is only valid for a smooth flow at the scale of the thickness of the diffuselet. In turbulence, this limits the applicability of the method to scales below the Kolmogorov scale, in the Batchelor regime. For instance, the length of a line element increases exponentially in time (like, say e^{Bt/τ_K} , see (1.2)) while the ‘box’ in which it is embedded has a size increasing only algebraically in time (like ϵt^3 typically, see (1.1)). Unavoidably, this diffuselet will overlap with itself at some point, filling the space in a compact fashion (Villermaux 2018), thus forcing self-overlaps and aggregation such as in confined mixtures (Duplat & Villermaux 2008). This phenomenon occurs in turbulent flows, but is not restricted to them, as it is a common feature of all random displacement fields whose small scales have a shorter turnover scale than larger ones (so-called rough flows), as in porous media (Le Borgne, Dentz & Villermaux 2015; Kree & Villermaux 2017) or dense suspensions (Turuban, Lhuissier & Metzger 2021) for instance. Again, the knowledge of the diffuselet is necessary, but not sufficient in that case to reconstruct the whole scalar field.

Finally, since this method is Lagrangian in its principle, it also suits heterogenous or chaotic flows. The presence of stable islands (see, e.g. Giona *et al.* 2004), separatrix or KAM torii is obviously taken into account by the trajectories of the diffuselets, because these sample all the sub-area of a given flow. This method thus permits us to solve mixing problems in flows with any degree of heterogeneity. However, the diffusion of scalar across barriers of transport (or separatrix) is not taken into account by this method. Periodic re-interpolations onto a regular grid as done in hybrid methods (Santoso *et al.* 2021; Leer *et al.* 2022) could solve this problem.

Funding. This project has received funding from the European Union’s Horizon 2020 research and innovation program under the Marie Skłodowska-Curie grant agreement N°956457.

Declaration of interests. The authors report no conflict of interest.

Author ORCIDs.

- ✉ Patrice Meunier <https://orcid.org/0000-0002-5034-6056>;
- ✉ Emmanuel Villermaux <https://orcid.org/0000-0001-5130-4862>.

Appendix A. Spectral DNS for a sine flow

The diffusion–advection with (2.1) of the concentration field by the sine flow is solved numerically using a spectral DNS code written on Matlab. The flow, given by (3.2) has a spatial wavelength equal to 1 and the filament has an initial length equal to 1. However, the filament is embedded in a 2-D space extending from 0 to 2π in each direction in order to model a solitary filament. We checked that the filament does not leave this region in the DNS. The concentration field $c(x, y, t)$ is modelled using its 2-D Fourier transform $\tilde{c}(k_x, k_y)$.

In the absence of advection, diffusion is easily applied at each time step by multiplying the concentration in the spectral domain $\tilde{c}(k_x, k_y, t)$ by a factor $\exp[-Dk^2\Delta t]$, with $k^2 = k_x^2 + k_y^2$ to get the concentration at time $t + \Delta t$. It should be noted that this solution is exact and, thus, valid for any Δt .

In the presence of advection, the advective term is usually calculated in real space,

$$N(x, y) = u(x, y)\mathcal{F}_{xy}^{-1}(ik_x\tilde{c}) + v(x, y)\mathcal{F}_{xy}^{-1}(ik_y\tilde{c}), \quad (\text{A1})$$

where \mathcal{F}_{xy}^{-1} corresponds to the 2-D inverse Fourier transform and i is $\sqrt{-1}$. This term is then transformed in Fourier space $\tilde{N}(k_x, k_y)$ and used to calculate \tilde{c} at time $t + dt$ using a

temporal scheme. For example, we have used a third-order Adams–Bashforth scheme for $\tilde{C}(k_x, k_y) = \tilde{c}(k_x, k_y)e^{Dk^2 t}$ which leads to the formula

$$\tilde{c}(t + \Delta t) = [\tilde{c}(t) - \frac{23}{12}\tilde{N}(t) + \frac{16}{12}\tilde{N}(t - \Delta t)e^{-Dk^2 \Delta t} - \frac{5}{12}\tilde{N}(t - 2\Delta t)e^{-Dk^2 2\Delta t}]e^{-Dk^2 \Delta t}. \quad (\text{A2})$$

This classical numerical simulation is used in the following as a reference simulation for moderate diffusivity $D = 10^{-5}$ and a small velocity $U = 0.3$. However, this simulation requires a very small time step Δt since the Courant–Friedrichs–Lowy (CFL) condition can be as small as 2×10^{-4} for $N = 8192$ (which is required for small diffusivity). Furthermore, we found that the scheme becomes rapidly unstable when D decreases. We have thus improved this classical method.

It is interesting to note that in the case of a sine flow, the velocity is invariant in the streamwise direction. For example, v is independent of y during the first step. It is thus convenient to work in a mixed space (x, k_y) . In the absence of diffusion, the advection equation for $\hat{c}(x, k_y)$ is written as

$$\frac{\partial \hat{c}(x, k_y, t)}{\partial t} = v(x)ik_y\hat{c}(x, k_y, t), \quad (\text{A3})$$

which can be integrated during each time step as

$$\hat{c}(x, k_y, t + \Delta t) = \hat{c}(x, k_y, t) \exp(i k_y v(x) \Delta t). \quad (\text{A4})$$

The link between $\hat{c}(x, k_y)$ and $\tilde{c}(k_x, k_y)$ is simply obtained by a one-dimensional Fourier transform in the x direction \mathcal{F}_x . Applying the diffusive damping to the final result leads to the formula

$$\tilde{c}(k_x, k_y, t + \Delta t) = \mathcal{F}_x[e^{ik_y v(x)} \mathcal{F}_x^{-1}(\tilde{c}(k_x, k_y, t))]e^{-Dk^2 \Delta t}, \quad (\text{A5})$$

which is applied for a given k_y and for all k_x simultaneously in order to calculate the discrete Fourier transform in k_x . It should be noted that this solution is exact in the absence of diffusion such that Δt could be taken as large as the period of step 1. However, in the presence of diffusion it is not equivalent to apply diffusion at the end or during the whole period such that Δt must be decreased, as we will show in the convergence study. In order to accelerate the convergence, the scheme is made symmetric by taking the mean between a diffusive operator at the end and at the beginning of each step,

$$\tilde{c}(k_x, k_y, t + \Delta t) = +\frac{1}{2}\mathcal{F}_x[e^{ik_y v(x)} \mathcal{F}_x^{-1}(\tilde{c}(k_x, k_y, t))]e^{-Dk^2 \Delta t} \quad (\text{A6})$$

$$+ \frac{1}{2}\mathcal{F}_x[e^{ik_y v(x)} \mathcal{F}_x^{-1}(\tilde{c}(k_x, k_y, t))e^{-Dk^2 \Delta t}]. \quad (\text{A7})$$

For the second step, similar arguments lead to the formula

$$\tilde{c}(k_x, k_y, t + \Delta t) = +\frac{1}{2}\mathcal{F}_y[e^{ik_x u(y)} \mathcal{F}_y^{-1}(\tilde{c}(k_x, k_y, t))]e^{-Dk^2 \Delta t} \quad (\text{A8})$$

$$+ \frac{1}{2}\mathcal{F}_y[e^{ik_x u(y)} \mathcal{F}_y^{-1}(\tilde{c}(k_x, k_y, t))e^{-Dk^2 \Delta t}]. \quad (\text{A9})$$

The concentration field obtained at $t = 15$ is plotted in figure 1 for $N = 8192$ Fourier modes in each direction and a time step $\Delta t = 0.005$. The convergence of this method has

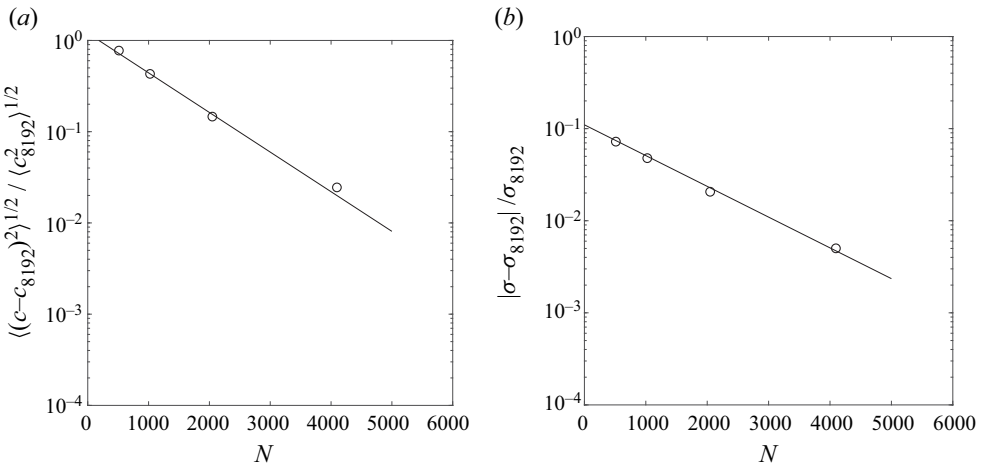


Figure 18. Convergence test as a function of the number of points N at time $t = 10$ for $U = 0.3$, $D = 10^{-6}$ and $\Delta t = 5 \times 10^{-3}$. The relative r.m.s. error on the total scalar field is plotted in (a) whereas the relative error on the standard deviation $\sigma = \langle c^2 \rangle^{1/2}$ is plotted in (b). The reference scalar field c_{8192} corresponds to the calculation with $N = 8192$.

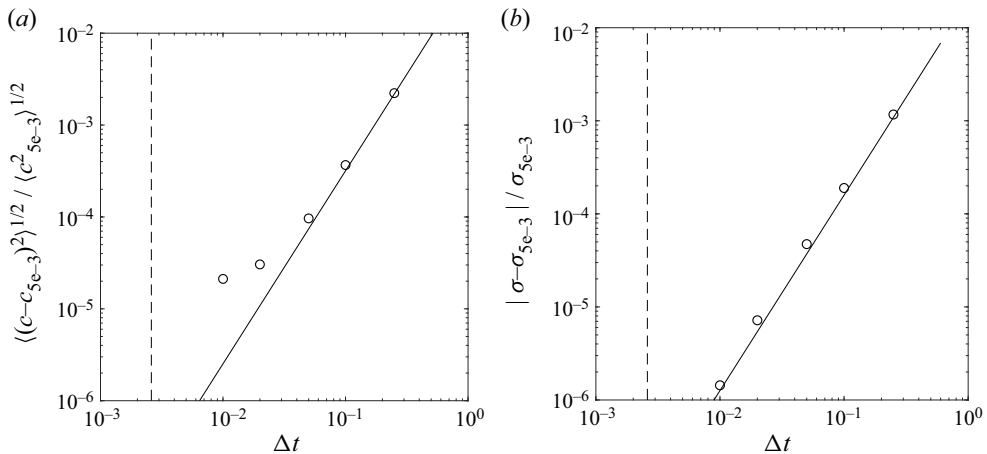


Figure 19. Convergence test as a function of the time step Δt at time $t = 10$ for $U = 0.3$, $D = 10^{-6}$ and $N = 8192$. The relative r.m.s. error on the total scalar field is plotted in (a) whereas the relative error on the standard deviation $\sigma = \langle c^2 \rangle^{1/2}$ is plotted in (b). The reference scalar field c_{5e-3} corresponds to the calculation with $\Delta t = 5 \times 10^{-3}$. The dashed line corresponds to the CFL condition and the solid line to a fit of the data as $\Delta t^{2.1}$.

been first quantified by decreasing the number of Fourier modes as shown in figure 18. It is clear that the root-mean-square (r.m.s.) error and the error on the standard deviation decrease exponentially as usually obtained for spectral codes. For $N = 8192$ modes, we can expect an error of the order of 0.1 % on the relative r.m.s. error and an error of the order of 0.02 % on the relative error of the standard deviation.

The convergence of the method has then been quantified by varying the time interval Δt as shown in figure 19. Both the r.m.s. error and the error on the standard deviation scale as $\Delta t^{2.1}$. If the scheme had been taken asymmetric (by applying the diffusive operator only at the end of each step), the error would scale as $\Delta t^{1.2}$. This method is thus of second

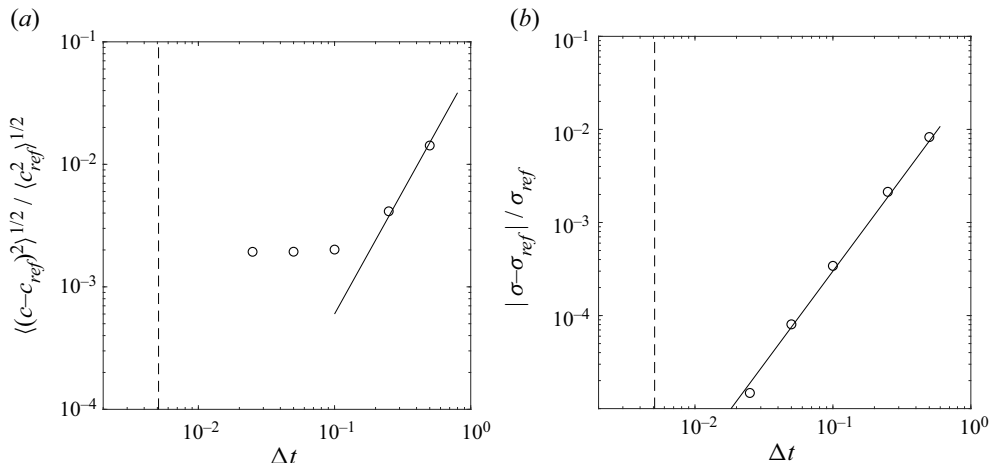


Figure 20. Convergence test as a function of the time step Δt at time $t = 10$ for $U = 0.3$, $D = 10^{-5}$ and $N = 4096$. The relative r.m.s. error on the total scalar field is plotted in (a) whereas the relative error on the standard deviation $\sigma = \langle c^2 \rangle^{1/2}$ is plotted in (b). The reference scalar field c_{ref} corresponds to a classic spectral DNS calculation with $\Delta t = 10^{-4}$ (i.e. 50 times smaller than the CFL) and a third-order Adams–Bashforth temporal scheme. The dashed line corresponds to the CFL condition and the solid line to a fit of the data proportional to Δt^2 .

order in its symmetric version. The most striking is that the r.m.s. error is of the order of 0.01 % for a time interval Δt of the order of 0.1, i.e. 50 times larger than the CFL condition. This error is extremely small and actually smaller than the error due to the finite number of Fourier modes. Furthermore, this method is extremely stable because the advection is simply a phase shift in the mixed space. All simulations were found to be stable even for a time interval equal to 0.5.

Finally, the method has been compared with a classical DNS using a third-order Adams–Bashforth time scheme (see above) with a time interval $\Delta t = 10^{-4}$, i.e. 50 times less than the CFL. Since the classical scheme is less stable, the comparison has been done for a smaller number of modes $N = 4096$ and a larger diffusion $D = 10^{-5}$. As shown in figure 20, the r.m.s. error and the error on the standard deviation decrease as Δt^2 . This indicates that there is no bias. For the r.m.s. error, the saturation at a relative error of 0.2 % is due to the error on the classical DNS rather than the error on our improved method.

REFERENCES

- AREF, H. 1984 Stirring by chaotic advection. *J. Fluid Mech.* **143**, 1–21.
 BALKOVSKY, E. & FOUXON, A. 1999 Universal long-time properties of lagrangian statistics in the Batchelor regime and their application to the passive scalar problem. *Phys. Rev. E* **60** (4), 4164–4174.
 BATCHELOR, G.K. 1952 The effect of homogeneous turbulence on material lines and surfaces. *Proc. R. Soc. Lond. A* **213** (1114), 349–366.
 BATCHELOR, G.K. 1959 Small-scale variation of convected quantities like temperature in turbulent fluid. Part 1. General discussion and the case of small conductivity. *J. Fluid Mech.* **5**, 113–144.
 BATCHELOR, G.K. & TOWNSEND, A.A. 1956 Turbulent diffusion. In *Surveys in Mechanics* (ed. G.K. Batchelor & R.M. Davies), pp. 352–399. Cambridge University Press.
 BRETHOUWER, G., HUNT, J.C.R. & NIEUWSTADT, F.T.M. 2003 Micro-structure and lagrangian statistics of the scalar field with a mean gradient in isotropic turbulence. *J. Fluid Mech.* **474**, 193–225.
 BUARIA, D., SAWFORD, B.L. & YEUNG, P.K. 2015 Characteristics of backward and forward two-particle relative dispersion in turbulence at different Reynolds numbers. *Phys. Fluids* **27** (10), 105101.

The diffuselet concept for scalar mixing

- CELANI, A., VILLERMAUX, E. & VERGASSOLA, M. 2014 Odor landscapes in turbulent environments. *Phys. Rev. X* **4** (4), 041015.
- COCKE, W.J. 1969 Turbulent hydrodynamic line stretching: consequences of isotropy. *Phys. Fluids* **12** (12), 2488–2492.
- CORRSIN, S. 1951 On the spectrum of isotropic temperature fluctuations in an isotropic turbulence. *J. Appl. Phys.* **22** (4), 469–473.
- CORRSIN, S. 1953 Remarks on turbulent heat transfer: an account of some features of the phenomenon in fully turbulent regions. In *Proceedings of the Iowa Thermodynamics Symposium*, pp. 5–30. State University of Iowa.
- CORRSIN, S. & KARWEIT, M. 1969 Fluid line growth in grid-generated isotropic turbulence. *J. Fluid Mech.* **39** (1), 87–96.
- DUPLAT, J., INNOCENTI, C. & VILLERMAUX, E. 2010a A nonsequential turbulent mixing process. *Phys. Fluids* **22** (3), 035104.
- DUPLAT, J., JOUARY, A. & VILLERMAUX, E. 2010b Entanglement rules for random mixtures. *Phys. Rev. Lett.* **105**, 034504.
- DUPLAT, J. & VILLERMAUX, E. 2000 Persistency of material element deformation in isotropic flows and growth rate of lines and surfaces. *Eur. Phys. J. B* **18** (2), 353–361.
- DUPLAT, J. & VILLERMAUX, E. 2008 Mixing by random stirring in confined mixtures. *J. Fluid Mech.* **617**, 51–86.
- ERTEL, H. 1942 Ein neuer hydrodynamischer wirbelsatz. *Meteorol. Z. (Braunschweig)* **59** (9), 277–281.
- FALKOVICH, G., GAWEDZKI, K. & VERGASSOLA, M. 2001 Particles and fields in fluid turbulence. *Rev. Mod. Phys.* **73** (4), 913–975.
- GIBSON, C.H. & SCHWARZ, W.H. 1963 The universal equilibrium spectra of turbulent velocity and scalar fields. *J. Fluid Mech.* **16** (3), 365–384.
- GIONA, M., ADROVER, A., CERBELLINI, S. & VITACOLONNA, V. 2004 Spectral properties and transport mechanisms of partially chaotic bounded flows in the presence of diffusion. *Phys. Rev. Lett.* **92** (11), 114101.
- GIRIMAJI, S.S. & POPE, S.B. 1990 Material-element deformation in isotropic turbulence. *J. Fluid Mech.* **220**, 427–458.
- GOLLUB, J.P., CLARKE, J., GHARIB, M., LANE, B. & MESQUITA, O.N. 1991 Fluctuations and transport in a stirred fluid with a mean gradient. *Phys. Rev. Lett.* **67** (25), 3507.
- GÖTZFRIED, P., EMRAN, M.S., VILLERMAUX, E. & SCHUMACHER, J. 2019 Comparison of Lagrangian and Eulerian frames of passive scalar turbulent mixing. *Phys. Rev. Fluids* **4**, 044607.
- HAYES, S.P., JOYCE, T.M. & MILLIARD, R.C. Jr. 1975 Measurements of vertical fine structure in the Saragasso Sea. *J. Geophys. Res.* **80** (3), 314–319.
- JAYESH & WARHAFT, Z. 1991 Probability distribution of a passive scalar in grid-generated turbulence. *Phys. Rev. Lett.* **67** (25), 3503.
- KRAICHNAN, R.H. 1974 Convection of a passive scalar by a quasi-uniform random field. *J. Fluid Mech.* **64** (4), 737–762.
- KREE, M. & VILLERMAUX, E. 2017 Scalar mixtures in porous media. *Phys. Rev. Fluids* **2**, 104502.
- LE BORGNE, T., DENTZ, M. & VILLERMAUX, E. 2015 The lamellar description of mixing in porous media. *J. Fluid Mech.* **770**, 458–498.
- LE BORGNE, T., HUCK, P.D., DENTZ, M. & VILLERMAUX, E. 2017 Scalar gradients in stirred mixtures and the deconstruction of random fields. *J. Fluid Mech.* **812**, 578–610.
- LEER, M., PETTIT, M.W.A., LIPKOWICZ, J.T., DOMINGO, P., VERVISCH, L. & KEMPF, A.M. 2022 A conservative Eulerian–Lagrangian decomposition principle for the solution of multi-scale flow problems at high Schmidt or Prandtl numbers. *J. Comput. Phys.* **464**, 111216.
- LUNDGREN, T.S. 1981 Turbulent pair dispersion and scalar diffusion. *J. Fluid Mech.* **111**, 27–57.
- MANABE, S. & WETHERALD, R.T. 1975 The effects of doubling the CO₂ concentration on the climate of a general circulation model. *J. Atmos. Sci.* **32** (1), 3–15.
- MARTÍNEZ-RUIZ, D., MEUNIER, P., FAVIER, B., DUCHEMIN, L. & VILLERMAUX, E. 2018 The diffusive sheet method for scalar mixing. *J. Fluid Mech.* **837**, 230–257.
- MEUNIER, P. & VILLERMAUX, E. 2010 The diffusive strip method for scalar mixing in two dimensions. *J. Fluid Mech.* **662**, 134–172.
- MONIN, A.S. & YAGLOM, A.M. (Edited by Lumley, J. L.) 1975 *Mechanics of Turbulence II*. The MIT Press.
- MUNK, W.H. 1966 Abyssal recipes. *Deep-Sea Res.* **13**, 707–730.
- OBUKHOV, A.M. 1941 On the distribution of energy in the spectrum of turbulent flow. *Bull. Acad. Sci. USSR, Geog. Geophys.* **5**, 453–466.
- ÖTTINGER, H.C. 1996 *Stochastic Processes in Polymeric Fluids*. Springer.
- OTTINO, J.M. 1989 *The Kinematics of Mixing: Stretching, Chaos, and Transport*. Cambridge University Press.

- PETERS, N. 1984 Laminar diffusion flamelet models in non-premixed turbulent combustion. *Prog. Energy Combust. Sci.* **10** (3), 319–339.
- PUMIR, A., SHRAIMAN, B.I. & SIGGIA, E.D. 1991 Exponential tails and random advection. *Phys. Rev. Lett.* **66** (23), 2984.
- RANZ, W.E. 1979 Applications of a stretch model to mixing, diffusion, and reaction in laminar and turbulent flows. *AIChE J.* **25** (1), 41–47.
- RICHARDSON, L.F. 1922 *Weather Prediction by Numerical Process*. Cambridge University Press.
- DE RIVAS, A. & VILLERMAUX, E. 2016 Dense spray evaporation as a mixing process. *Phys. Rev. Fluids* **1** (1), 014201.
- ROTHSTEIN, D., HENRY, E. & GOLLUB, J.P. 1999 Persistent patterns in transient chaotic fluid mixing. *Nature* **401**, 770–772.
- SALAZAR, J.P.L.C. & COLLINS, L.R. 2009 Two-particle dispersion in isotropic turbulent flows. *Annu. Rev. Fluid Mech.* **41**, 405–432.
- SANTOSO, S., LAGAERT, J.-B., BALARAC, G. & COTTET, G.-H. 2021 Hybrid particle-grid methods for the study of differential diffusion in turbulent flows. *Comput. Fluids* **227**, 105018.
- SCHWERTFIRM, F. & MANHART, M. 2007 DNS of passive scalar transport in turbulent channel flow at high Schmidt numbers. *Intl J. Heat Fluid Flow* **28** (6), 1204–1214.
- SHRAIMAN, B.I. & SIGGIA, E.D. 2000 Scalar turbulence. *Nature* **405** (6787), 639–646.
- SIMONET, C. & GROISMAN, A. 2005 Chaotic mixing in a steady flow in a microchannel. *Phys. Rev. Lett.* **94**, 134501.
- SREENIVASAN, K.R., TAVOURALIS, S., HENRY, R. & CORRSIN, S. 1980 Temperature fluctuations and scales in grid-generated turbulence. *J. Fluid Mech.* **100** (3), 597–621.
- SUKHATME, J. & PIERREHUMBERT, R.T. 2002 Decay of passive scalars under the action of single scale smooth velocity fields in bounded two-dimensional domains: from non-self-similar probability distribution functions to self-similar eigenmodes. *Phys. Rev. E* **66**, 056302.
- TAVOURALIS, S. & CORRSIN, S. 1981 Experiments in nearly homogenous turbulent shear flow with a uniform mean temperature gradient. Part 1. *J. Fluid Mech.* **104**, 311–347.
- TURUBAN, R., LHUISSIER, H. & METZGER, B. 2021 Mixing in a sheared particulate suspension. *J. Fluid Mech.* **916**, R4.
- VILLERMAUX, E. 2018 On shapes and forms: population balance dynamics of corrugated stirred fronts. *C. R. Phys.* **19** (5), 306–315.
- VILLERMAUX, E. 2019 Mixing versus stirring. *Annu. Rev. Fluid Mech.* **51**, 245–273.
- VILLERMAUX, E., STROOCK, A.D. & STONE, H.A. 2008 Bridging kinematics and concentration content in a chaotic micromixer. *Phys. Rev. E* **77** (1, Part 2), 01533301.
- WANG, L. & PETERS, N. 2006 The length-scale distribution function of the distance between extremal points in passive scalar turbulence. *J. Fluid Mech.* **554**, 457–475.
- WARHAFT, Z. 2000 Passive scalars in turbulent flows. *Annu. Rev. Fluid Mech.* **32** (1), 203–240.
- WUNSCH, C. & FERRARI, R. 2004 Vertical mixing, energy, and the general circulation of the oceans. *Annu. Rev. Fluid Mech.* **36**, 281–314.
- YEUNG, P.K. 2002 Lagrangian investigations of turbulence. *Annu. Rev. Fluid Mech.* **34**, 115–142.
- YEUNG, P.K., DONZIS, D.A. & SREENIVASAN, K.R. 2005 High-Reynolds-number simulation of turbulent mixing. *Phys. Fluids* **17**, 081703.